Terahertz Time-Domain Spectroscopy for Characterizing Properties of Carbon Nanotube Yarns

A Major Qualifying Project
Submitted to the Faculty of
WORCESTER POLYTECHNIC INSTITUTE
in partial fulfillment of the requirements
for the Degree of Bachelor of Science in

Applied Physics

By:

Natalie Frey

Project Advisors:

Professor Kateryna Friedman
Professor Lyubov Titova

Date: March 2024

Abstract

Carbon nanotube (CNT) yarns are made of aligned filaments of structured carbon, such as single or multi-walled carbon nanotubes. They have many advantageous properties, such as their flexibility, strength, and thermal and electrical conductivity. This makes high quality CNT yarns desirable in many applications. Here we report on using THz time-domain spectroscopy (THz-TDS) to characterize Miralon® yarn manufactured by Huntsman Corporation. As CNTs strongly absorb and reflect THz radiation polarized along the CNT axis, THz-TDS provides a rapid, non-destructive approach to characterize CNT fiber bundle alignment in the yarn materials. In this report, THz-TDS measurements of two yarn samples with differing strengths were compared to find a correlation between THz absorption and yarn tenacity. It was found that the stronger yarn had more uniformity in THz absorption across multiple spots, meaning higher uniformity in the CNT bundle alignment within the yarn plays a key role in yarn strength.

Acknowledgements

I would like to thank Professor Titova for getting me involved in the project and giving me the opportunity to work in the THz and Spectroscopy Lab. I would also like to thank Professor Friedman for her support throughout the project and assistance writing this report. I couldn't have completed this without their support and guidance. Thank you to my Dad, as well, for helping me when my MATLAB code didn't work.

Thank you to Nanocomp Technologies, Inc. for providing the CNT yarns. Thank you to the Center for Industrial Mathematics and Statistics at WPI for providing the REU site, and to the National Science Foundation for funding it.

Contents

1 Introduction

Carbon nanotubes (CNTs) are made of a hexagonal array of carbon atoms, graphene, in the form of a tube or cylinder, seen in figure 1. CNTs could be single-walled, with a diameter of less than 1 nm, or multi-walled, consisting of multiple concentrically interlinked nanotubes, in this case their diameters may exceed 100 nm. Additionally, CNTs could reach several micrometers and even millimeters in length scale. This unique structure and strong van der Waals interactions gives CNT materials their unique and beneficial properties, such as high elastic modulus and strength comparable to steel with a fraction of the density, as well as high electrical and thermal conductivity. CNTs have the highest breaking length of any meaningful conductor, which makes them important for applications with high instantaneous loads, high gravitational or other forces. High conductivity allows CNTs to carry a substantial amount of power for multiple implementations, such as satellites. These unique properties make CNTs an attractive material for numerous applications in many industries [1].

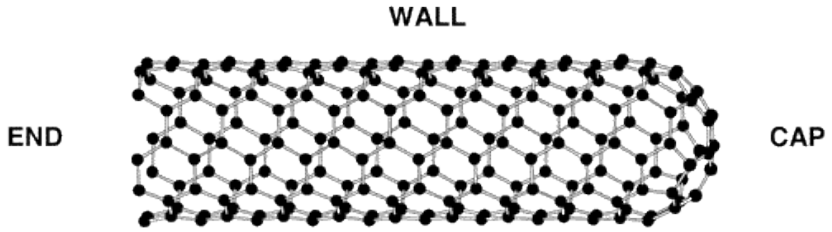

Figure 1: Single-walled carbon nanotube. Reprinted with permission from [2]. Copyright 2002, American Chemical Society

For this project we were collaborating with Huntsman Corporation. Specifically, we were looking at their Miralon® carbon nanotube materials, which are made into sheets, tapes, fillers, and yarns, making them extremely versatile. Here, we focused our study on Miralon® carbon nanotube yarns, which are made of millions of CNTs bundled into a thread-like material. There are many different methods that have been used to characterize the properties of CNTs. One of them is tensile strength measurement, the maximum amount of force a material can undergo before breaking. In this method, the force is measured by pulling on the CNTs until they break apart, the tensile strength of CNT yarns is commonly measured this way. However, when it comes to commercially sold CNT yarn, like Miralon®, this test method then renders the product unusable.

Terahertz time-domain spectroscopy (THz-TDS) is a unique non-destructive technique that allows us to study various properties of the materials. THz radiation is found between infrared and microwave ranges of the electromagnetic spectrum, as shown in the Fig. 2. The THz region includes frequencies from 100 GHz to 10 THz on the electromagnetic spectra. In other units the THz region can be defined as 30 μm – 3000 μm (wavelength) or 3.33 cm^{-1} –333 cm^{-1} (wavenumber). Many materials produce a unique spectrum in this range and also exhibit unique material properties, such as free carrier absorption, carrier-carrier scattering, plasma formation in semiconductors, lattice vibrations in solids, exciton orbital transitions, and many others. All this allows for the study of unique and useful material properties in THz range [3]. Additionally, the THz-TDS technique is used in many industries, particularly for quality control. THz pulses pass through many materials that don't appear transparent to the human eye, making it good for non-invasive and non-destructive imaging technique. It is also commonly used in airports for security, since it may image through clothes to reveal weapons.

Here we will apply THz-TDS technique to characterize the strength of the CNT yarns. Previously, Ren et al. (2012) demonstrated that a film of near perfectly aligned CNTs exhibits properties of an

ideal polarizer for the THz range. The van der Waals forces that hold the CNTs together within in the yarn are highly dependent on the distance between the tube [4]. Increased alignment of the CNTs within the yarn will have stronger polarizability in THz range and may be a sign of increased strength in the CNT yarn, providing a new non-destructive test method for commercially produced CNT products.

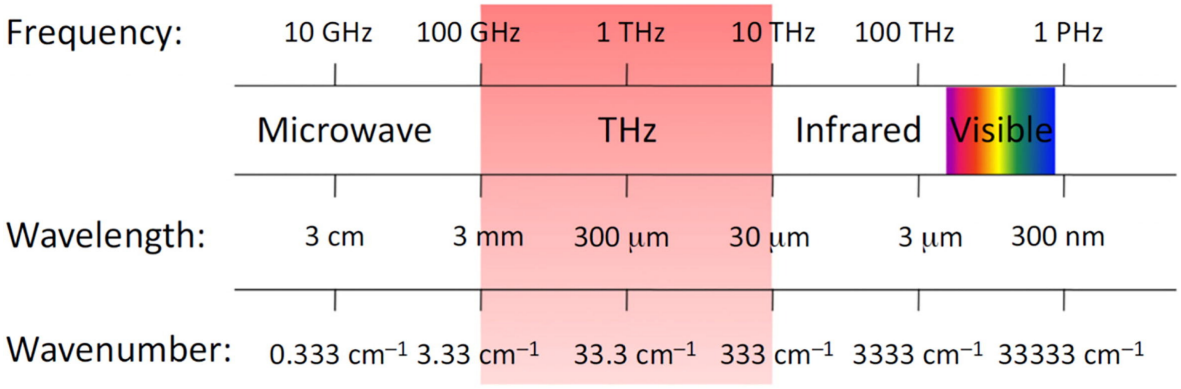

Figure 2: THz region on the Electromagnetic spectrum [5]

2 Background

2.1 Carbon Nanotubes

Carbon nanotubes consist of long, slender fullerenes, C_{60} molecules, with walls of the tubes are hexagonal carbon (graphite structure) and often capped at each end. Carbon nanotubes were first observed in 1991 by Iijima [6]. Since then, many investigations of their remarkable mechanical and physical properties, like their high tensile strength and conductivity. These properties of CNTs have led to their fabrication into sheets, fillers, or yarns.

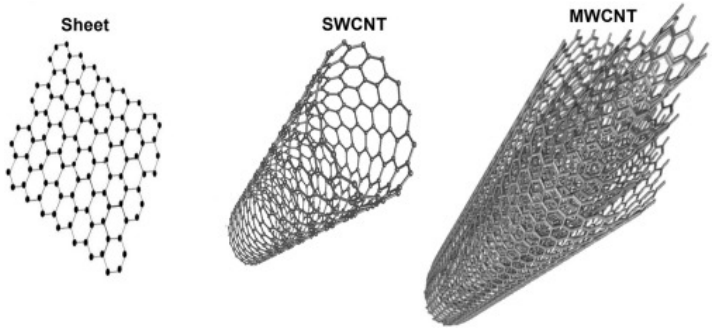

Figure 3: Sheet of carbon atoms, Single-walled CNT, and multiwalled CNT. Reprinted from [7], with permission from Elsevier

2.1.1 Structure

To better understand the properties of the Carbon nanotubes, it is important to look at their structure. The structured carbon within a carbon nanotube can be imagined as a hexagonal array of carbon atoms that have been rolled up into a tube. This structure can then be described using the chiral, or "roll-up", vector, which can be seen in figure 4. The following equation can be used to describe the chiral vector,

$$\vec{C_h} = n\vec{a_1} + m\vec{a_2} \tag{1}$$

$\vec{C_h}$ represents the chiral vector, while $\vec{a_1}$ and $\vec{a_2}$ are unit vectors, and (n, m) are integers. The angle θ between $\vec{a_1}$ and $\vec{a_2}$ is the chiral angle, which is how "twisted" the tube is. There are two special cases in nanotube geometry. When $(n, 0)$ and the chiral angle is $0°$ the geometry is called "zigzag". The other case is "armchair" which occurs when (n, n) and the chiral angle is $30°$. Tube chirality has a large impact on the electronic properties. Graphite is known to be semimetal, but carbon nanotubes can be either metallic or semiconducting, depending on the tube chirality. Specifically, when $(n-m)/3$ is an integer the tube will have metallic properties, in all other cases the tube will be semiconducting [1] [8]. CNTs may be further classified as single walled (SWCNTs) or multiwalled (MWCNTs), shown in figure 3. In the case of MWCNTs, they are made of multiple concentric SWCNTs. Each of the tubes making up the MWCNTs can have different chirality [7].

While carbon atoms within the CNTs are held together with sp^2 hybridized covalent bonds, the layers in MWCNT are held together by van der Waals forces. This creates a small separation distance between layers in MWCNTs while also bonding them together [7]. The van der Waals interaction is an electrostatic force that occurs when two neutral particles are within a certain distance. The electrons from one particle are attracted to the nucleus of the other. The induced dipoles result in an attraction between the atoms and a repulsive interaction when the particles get too close and their electron clouds

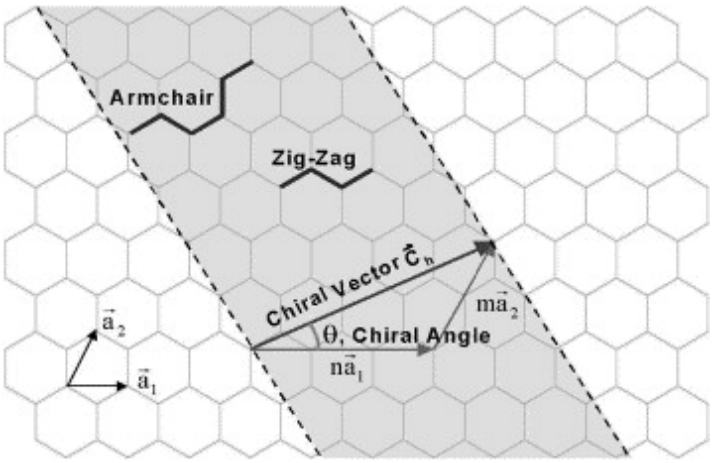

Figure 4: Diagram depicting the chiral vector on a hexagonal sheet. Reprinted from [1], with permission from Elsevier

overlap. The force is weaker and sensitive to the distance between particles, since it is not the result of a chemical bond [4]. This causes the junctions between CNTs to experience reduced mechanical strength and conductance[9].

The van der Waals interaction force between two atoms or small molecules can be described using the Lennard-Jones potential. Generally, the Lennard-Jones description of van der Waals energy for carbon nanostructures is defined in the following way:

$$V(x) = 4\epsilon \left[\left(\frac{\sigma}{x}\right)^{12} - \left(\frac{\sigma}{x}\right)^{6} \right] \tag{2}$$

With $\epsilon = 2.84$ meV and $\sigma = 3.403$ Å [10]. Additionally, the van der Waals force at the contact point of two MWCNTs (P) can be estimated with the following equation:

$$P = \frac{3\pi d_{max} E({D_o}^4 - {D_i}^4)}{64{L_1}^3} \tag{3}$$

Here, d_{max} is the deflection at the point of contact between the MWCNTs, E is the Young's modulus. D_o, D_i, and L_1 is the outer diameter, inner diameter, and L_1 the length of the MWCNT, respectively [9]. Models of CNTs using Lennard-Jones potential have shown how the diameter and spacing of the CNTs may impact the elastic modulus, also depending on the array size and structure [11]. However, when the diameter of the CNT increases too much, the tube may collapse due to the present van der Waals force. It is also responsible for the self-assembly habits and bonding of multiple CNTs within clusters, with the measured cohesive force between CNTs ranging between 1.7 to 8.5 nN [9]. The stability of formed CNT structures may improve when there is more order in the array [10].

2.1.2 Synthesis and Growth

There are four main methods for the synthesis of CNTs: laser ablation, arc-discharge, gas-phase catalytic growth, and chemical vapor deposition (CVD) using hydrocarbons [1]. In the laser ablation process, a high-intensity laser strikes a graphite surface inside a chamber filled with helium or argon gas. The graphite is vaporized, and then collected and cooled. When the vapor cools, the molecules stabilize and form clusters of CNTS [12]. Arc-discharge synthesis involves a chamber with a helium atmosphere and two thin electrodes placed in the center. A DC current runs in the electrodes, made

of graphite, and an arc generates between them [13]. The anode gets consumed and the CNTs are deposited on the cathode. Due to the limited size of the initial carbon target, these techniques are difficult to scale up for large scale production of CNT. Therefore, laser ablation and arc discharge are not often used for the production of CNTs for commercial applications. An additional step is often required for these techniques for further refinement, since they often leave behind many impurities such as amorphous carbon and catalyst particles [1].

Gas-phase catalytic creation can be used for continuous growth of SWCNTs with the use of a flowing feedstock mixture. The highest yield of CNTs was using carbon monoxide, CO, as the feedstock and iron pentacarbonyl, $Fe(CO)_5$, as the precursor catalyst. As the feedstock and a small amount of the catalyst flow into a heated reactor. The $Fe(CO)_5$ goes through thermal decomposition, and the products react and from gas phase iron clusters. CNTs then grow on these clusters through CO disproportionation [14]. CVD has the best potential for scaling up to produce large amounts of CNTs. Compared to other methods, it has a higher production output and operates at lower temperature and pressures. A hydrocarbon vapor with metal nanoparticles enters a hot reactor. The reaction separates the hydrocarbon into individual carbon and hydrogen. The carbon is collected on a solid metal surface and crystallizes into a CNT. The crystallization of the carbon absorbs the heat that is created on the metal surface from the hydrocarbon breakdown, helping sustain the creation process, and CNT will grow continuously as long as the metal surface is available [15].

2.1.3 Properties

Due to the carbon-carbon sp^2 bonding, CNTs have high stiffness and axial strength [16]. Being stiff yet flexible, CNTs appear to behave as ideal carbon fibers[17]. The elastic modulus for MWCNT's ranges from 270 to 950 GPa, and 320 to 1470 GPa for bundles of SWCNTs. The measured tensile strengths are 11-63 GPa and 13-52 GPA, respectively. [1]. Looking at commercial carbon fiber for comparison, its elastic modulus ranges from 200-500 GPa and the tensile strength ranges from 3-7 GPa [18]. The elastic modulus for MWCNTs does depend on the amount of "disorder" within the CNT walls, as the disorder increases the elastic quality of the tube decrease [17]. CNTs are subject to a unique mechanical failure of sliding/telescoping. When MWCNT bundles are under tensile stress, the outermost tube fails first, followed by the inner tubes being pulled out [1].

Thermal and electrical properties of CNTs are highly anisotropic, with the electrical and thermal conductance being highest along the CNT axis. It has been shown that when the alignment of SWCNTs increases, both thermal and electrical conductivity along the axis of the CNT increases [19]. At room temperature, the thermal conductivity falls above 2000 W/mK for SWCNTS, and about 3000 W/mK for MWCNTS, making the material comparable to diamond [20]. CNTs were found to be thermally stable up to 2800°C in a vacuum [1]. Compared to other properties of CNTs, the thermal properties have been less explored, but it has been shown that the connections and alignment between CNTs may affect the thermal conductivity [21].

CNTs have high electrical conductance and low resistance. Measuring these properties can be difficult, due to the dependence on tube geometry. As mentioned prior, the chirality of the CNTs causes them to be either metallic or semiconducting, meaning their measured resistance to vary by orders of magnitudes between tube[22]. The carbon atoms are arranged in a hexagonal lattice, meaning each atom is covalently bonded to three neighboring carbon atoms with the sp^2 molecular orbitals and the fourth valence electron in each is left free. The free electron from all the atoms contribute to the electrical properties of the CNTs, resulting in either conducting or semi-conducting CNTs [13]. Semiconducting SWNTs are usually in the form of p-type semiconductors [23]. Additionally, since

MWNTs are composed of layers of different SWNTs, they are likely to be strictly one-dimensional conductors. Going further, structural elements in self-assembled CNT bundles, like tube alignment and entanglement, also cause variation in resistivity and conductivity. Impurities like amorphous carbon left over in the tubes from synthesis increase the resistivity seen in the bundle [21]. There is a wide range of measured resistances of CNTs, for example, metallic SWNTs resistance ranges from 0.34×10^{-4} to 1.0×10^{-4} ohm·cm [22]

Tube diameter also affects the electronic properties. Smaller tubes may have decreased energy gaps and the conductive behavior may be different than the prediction based on the tube chirality. Ultra-small diameter tubes may even display superconductive behavior [24]. When compared to copper wires, their current carrying capacity is about 1000 times higher. CNTs achieve all of these properties while maintaining a very low density in comparison with the materials of similar qualities [1]. When compared to other common conductors, seen in figure 5, they have the highest breaking length by far, making them useful in applications where they would see high forces or loads. Their high conductivity and aspect ratio makes them useful as conducting composites. Compared to carbon black, a commonly used composite, the same conductance may be achieved with CNTs using a significantly smaller amount of the material [25]. Electrical properties of both SWNTs and MWNTs have been relatively well explored due to the growing interest in their applications. This gives us the opportunity to use this knowledge in characterizations of our CNT yarns.

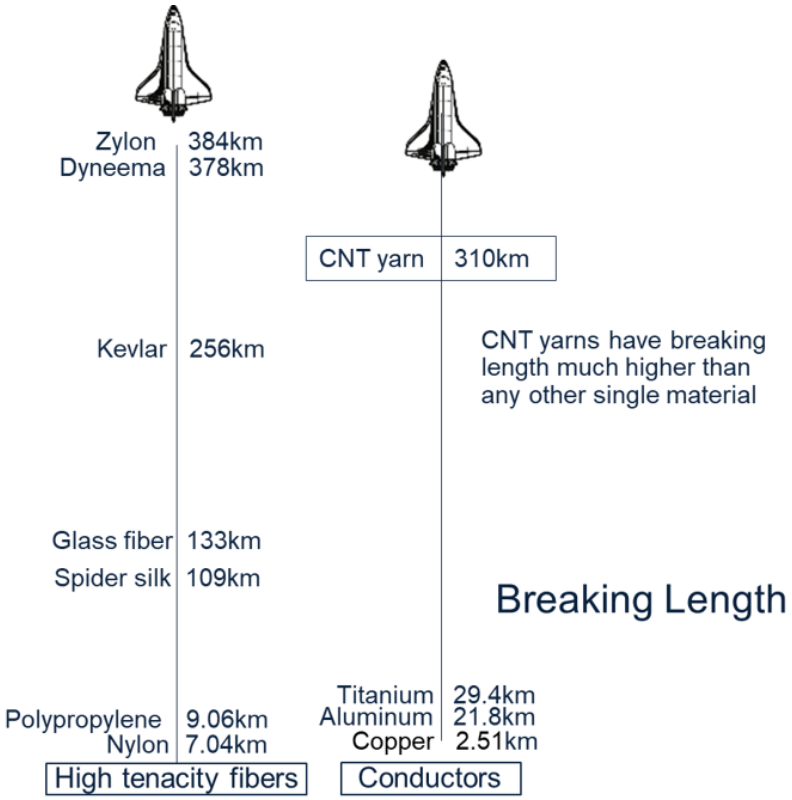

Figure 5: Breaking length of high tenacity fibers and conductors compared to CNT yarn. Image provided by Nanocomp Technologies, Inc.

2.1.4 Characterization Techniques

Transmission electronic microscopy (TEM) and scanning tunneling microscopy (STM) are able to investigate the structure and properties of individual nanotubes. TEM utilizes a beam of electrons that are transmitted through a material to form an image. It provides a view of a microstructure and atomic arrangements through measuring variations between regions [26]. For CNTs, it can be used to study the structure, thickness, diameter, and shell spacing in MWCNTs [27]. The structure and helicity of CNTs within packed bundles may be determined when TEM is used with electron diffraction [28].

A unique aspect of STM is that the structural and electronic characteristics may be measured simultaneously. The CNTs are deposited on a conducting substrate, and the three-dimensional atomic structure and density of state may be resolved [28]. STM was used to confirm the structure of the CNTs and the difference in conductivity depending on tube chirality. CNT helicity may be determined from STM measurements using the nanotube diameter and the chiral angle. Keeping the STM tip stationary and recording the current through the CNT as a function of current allows for the electronic properties to be characterized. This variation of the technique, called scanning tunnel spectroscopy (STS), is one of the routine methods for measuring tube radii. Using STS along with STM allows for a complete characterization of CNT structure [29].

Other techniques like x-ray diffraction, infrared and Raman spectroscopy are available as global characterization techniques. It can be used for statistical characterization of CNTs and can obtain information about impurities, structural strain, and layer spacing [28]. X-ray diffraction makes use of x-rays generated in a cathode ray tube that pass through the material, causing them to diffract. The angles and intensity of the diffracted beams are measured. The diffraction patterns of CNT are similar to those of graphite and graphene, making it difficult to differentiate the structures. It is useful for determining the purity of CNTs, as the impurities shift the locations of the peaks in the diffraction pattern. The amount of layers in the CNT may be identified using the noise ratio [30]. Spectra of CNT from infrared spectroscopy also show strong similarities to that of graphite. Comparisons of TEM and infrared spectroscopy measurements have allowed for structural properties to be characterized using the spectral properties. Nanotube diameters, vibrational modes, and purity can be obtained based on observed intensity, bandwidth, and peaks in the spectrum [31].

Raman spectroscopy is one of the most common characterization tools used for CNTs, producing a lot of information on their vibrational and electronic properties. Minimal sample preparation is required, so faster analysis is possible [28]. CNTs exhibit a unique radial breathing mode due to radial vibration of the carbon atoms. The frequency of this breathing mode has been used to identify the diameter of the CNT, and its intensity can be used to study the electronic structure [32]. The tangential mode is called the G-band, after graphite. While it is less accurate than radial breathing mode analysis, G-band peaks and separation can be used to measuring CNT diameter. Zig-zag and armchair CNTs have differing numbers of modes present in the G-band, so tubes may be identified as metallic or semiconducting through its study [33].

2.1.5 Carbon Nanotube Yarns

CNT yarn is made up of millions of bundles of CNTs that have been pulled together and stretched into a long, thread-like material. One way to visualize this is by comparing the CNT yarns to wool knitting yarns. Wool knitting yarns are made of wool fibers that spun to form a continuous length. While very different materials, the principle is similar in that the CNT bundles are like the wool fibers and are "spun" together to form the CNT yarn.

Applications of CNT yarns include their use as capacitive electrodes for electrochemical water treatment and energy generation. The length, flexibility, strength, and conductance of the yarn may lead to the development of new electrode designs with higher energy efficiency and lower environmental impact [34]. They are promising for the production of wearable electronics [35], and have been used in textiles, being made into multiple yarn structures or braids. While this does not increase the mechanical strength, it makes them more easily implemented into composite materials or textile structures [36]. Piezoresistive strain sensors have been made with CNT yarns, to monitor metallic or composite structures. There is also the possibility of building these sensors into the structure for continuous damage and strain monitoring [37]. Their length, flexibility, strength, and conductivity is what sets them apart from other materials and makes them promising in many applications.

Miralon® CNT products are manufactured by Huntsman Corporation. The Miralon® CNT materials are made into multiple different products, including sheets, tapes, and the yarns. The material is extremely versatile, making them useful in many commercial industries, such as automotive, construction, and aerospace [38]. Miralon® CNT sheets were integrated into NASA's Juno spacecraft to provide protection against electrostatic discharge. Additionally, in 2016 NASA was also looking into using Miralon® Yarn as reinforcement on an aluminum tank, seen in figure 6 [39].

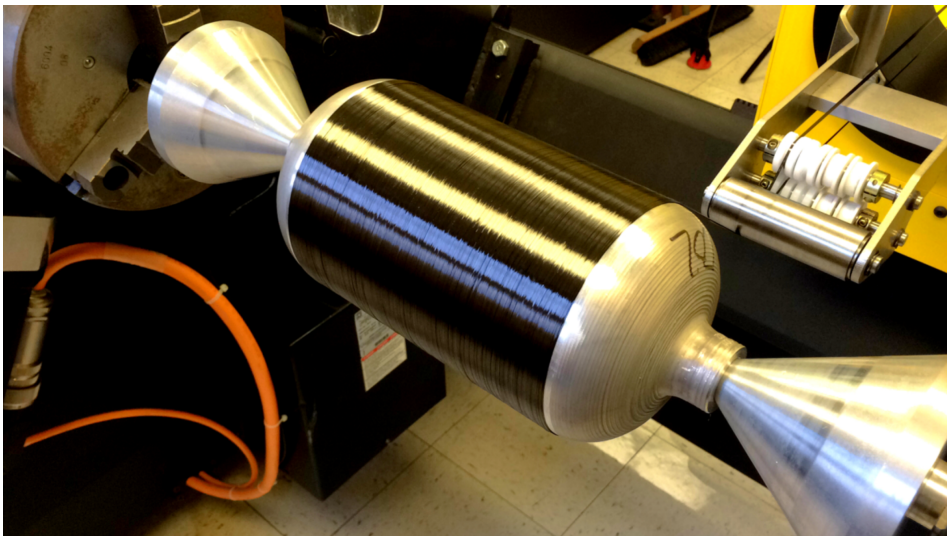

Figure 6: NASA Flight article wrapped with a CNT Composite [40].

The production method used for Miralon® products takes natural gas or other hydrocarbons and separates them into the material and clean hydrogen. Carbon nanotubes are synthesized using a gas phase pyrolysis process, shown schematically in figure 7. This is similar to the CVD process, but a metal organic compounded is added to the carbon based fuel, the furnace uses is seen in figure 8. Growth of catalyst particles are stopped when they reach a certain size. At some point in the process, the tubes form bundles through electrostatic attraction. A cloud of these bundles then exit the furnace and are manipulated to form yarns or sheets. To form the yarns, the cloud is collected on a substrate

and then pulled off into a spinning device [41]. The yarns also go through an additional processing step where the yarn is chemically treated, flattened, and drawn out.

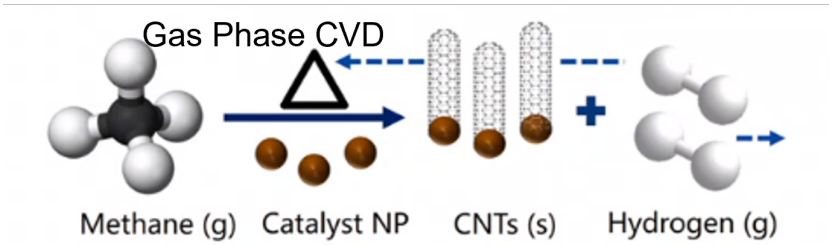

Figure 7: Gas phase CVD production method for CNTs. Image provided by Huntsman Corporation

An interesting aspect of the Miralon® manufacturing process is the creation of clean hydrogen as a byproduct. The need for hydrogen worldwide has increased drastically, with one reason being the growing interest in its use in clean energy systems. However, the production of hydrogen is responsible for about 830 million tonnes of carbon dioxide emissions, meaning there is a desire for cleaner production method of hydrogen [42] [43]. Compared to a traditional method of creating hydrogen, Steam Methane Reforming, it was found that the Miralon® production process can reduce the carbon footprint by up to 90 percent by creating the useful carbon product as one of the outputs [38].

A study by Downes et al. (2015) assessed the self-assembly habits and failure modes of Miralon® CNT products, specifically CNT sheets. A common structure formed by CNT self-assembly is a flattened stack, where tubes with larger diameters will collapse, while smaller ones will remain cylindrical. Figure 9 shows TEM images of stacks of CNTs with varying amounts of collapsed, partially collapsed, and non-collapsed CNTs. Stacks of these flattened tubes have a higher surface and contact area and a higher density. The stacks are predicted to have a higher strength as CNT to CNT bond is critical for increasing mechanical strength. Despite this, the stacks are still found to experience the major "telescoping" failure mode, where bundles are found to be progressively pulled out until ultimate failure. Figure 10 shows the different failure modes that were observed for the stacks. The bundle pull-out failure mode is key in understanding the strength of the yarns, as it was predicted that increasing alignment would increase the tensile strength. Increasing the CNT to CNt bond is critical to increasing the mechanical strength [44].

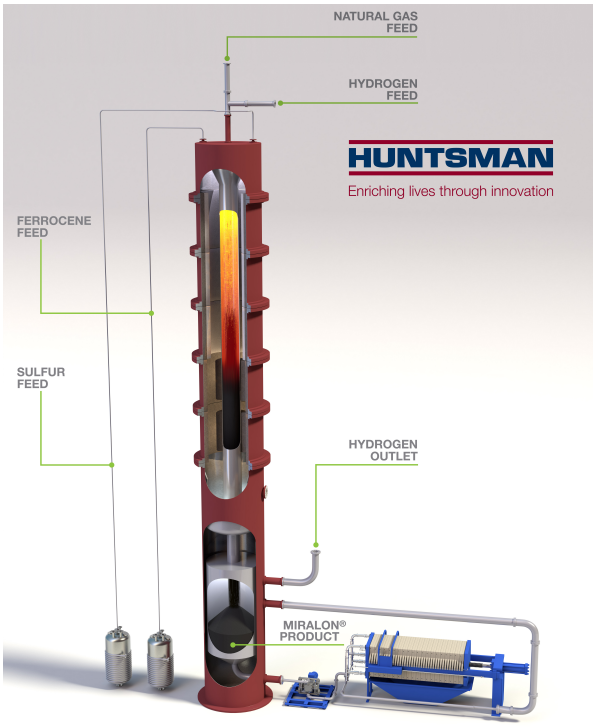

Figure 8: Schematic of Furnace used by Huntsman Corporation to manufacture CNT products [38].

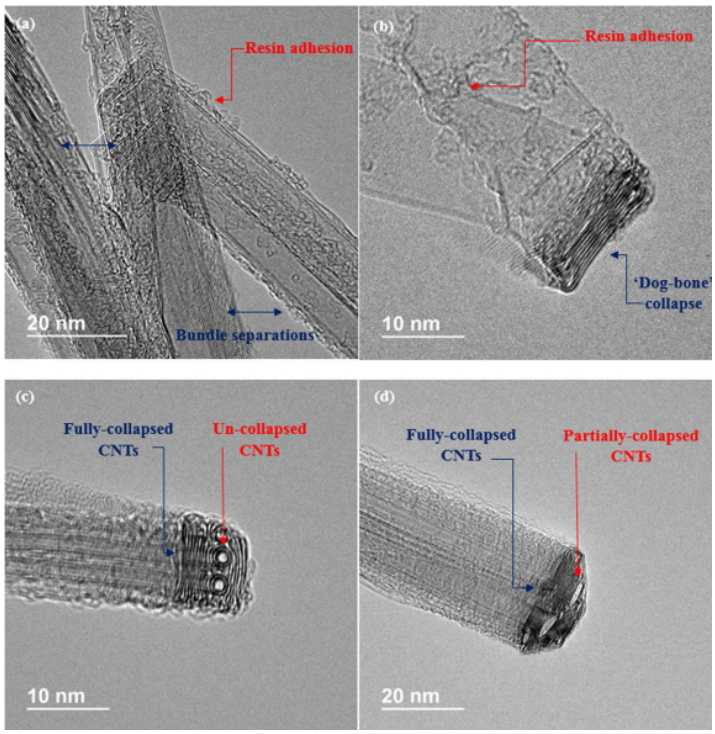

Figure 9: TEM images of self-assembled CNT stacks. a) Resin adhesion and CNT bundle separation b) Collapsed CNT stack c) Collapsed large-diameter CNTs, non-collapsed small-diameter CNTs d) stack partially collapsed and fully collapsed CNTS. Reprinted from [44], with permission from Elsevier.

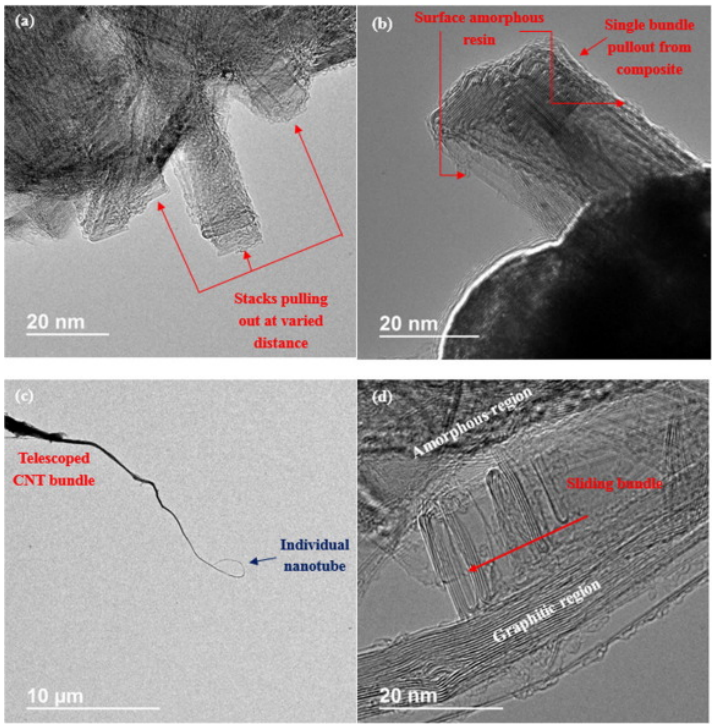

Figure 10: TEM images of CNT stack failure modes a) individual pullout of stack b) whole stack pullout c) stack telescoping pullout d) single flattened stack sliding pullout. Reprinted from [44], with permission from Elsevier.

Quality control for the CNT yarns ensures consistency of properties between batches of yarns. While much is known about the synthesis of CNTs, little is known about how different changes in the manufacturing process affects the yarns properties. Small changes in the process can vastly affect the tensile strength of a created yarn. The current method used to test and measure the tensile strength of the yarn is to pull at the ends until it fails. This then renders the product useless and unsellable. There is a need for a new test method to characterize the yarns, one that is non-destructive and allows for quick measurements to be made over multiple spots on the same yarn.

2.2 Technique

In the electromagnetic spectrum, terahertz (THz) radiation is found in between infrared and microwaves and are typically defined as being between 3000μm (100 GHz) and 30μm (10 THz), as shown in the Fig.2. While this region was relatively unexplored until recently, it has many interesting properties that make it a popular choice for spectroscopy applications. Applications can be found in various fields such as material science [45] [46], biomedical [47], information technology and communications[48], homeland security [49], quality control [50] [51], and many others.

Here we are interested in the material science application of the THz spectroscopy. Many materials have a unique spectral fingerprint in this range, which can then be used to identify them. Some materials may also appear as transparent in the THz region, even when appearing opaque to the human eye [3]. 1 THz corresponds to a photon energy of 4.1 meV, which is smaller than the characteristic thermal energy of $k_bT = 25meV$ at room temperature, and smaller than the typical band gap of a semiconductor. Which means that THz pulses are perfect for low-energy excitations [52], such as free carrier absorption [53], carrier scattering [54], plasma formation [55], lattice vibrations in solids [56],

exciton orbital transitions [57] [58] and others.This has made THz spectroscopy a valuable tool for condensed matter physics and materials science.

The most common THz spectroscopy techniques are Time-Domain spectroscopy (THz-TDS), THz emission spectroscopy (TES), Time-Resolved THz spectroscopy (TRTS). Each technique has their own benefits and applications, more information can be found elsewhere [59] [60]. We will focus on the THz-TDS technique. THz-TDS is used for non-invasive and non-destructive characterization of materials. Unlike most other optical spectroscopy modalities, THz-TDS records the transient electric field rather than the intensity [61]. THz pulses used to probe materials properties, a recorded in the time-domain, as electric field as function of time [62]. Data may be analyzed in either the time-domain, or the frequency domain if a Fourier transform is performed. The short pulses and coherent detection methods used allow for direct measured of the electric field amplitude and phase, which allows for the absorption coefficient and refractive index of a material to be measured [63]. Additionally, if a Fourier transform is done, the complex-valued refractive index may be calculated from the spectral data [61].

There have been advances in using THz-TDS to detect macromolecules, such as carbohydrates, proteins, amino acids, and nucleic acids. In protein detection, THz-TDS may provide insight into the molecular conformation and interactions as well as quantitative detections. THz-TDS is sensitive to conformation and mutations of biomolecules, as conformational changes directly affect the dielectric response in the THz range [5]. Due to the low energy of THz photons, biological tissue is not harmed, making it useful for assessing the internal structure of macromolecules [64].

For industrial applications, THz-TDS systems have been used in the inspection of plastic components, revealing defects such as voids, deformations, and thermal or mechanic stress within polymer materials. Properties of composites materials can be determined with their refractive index and absorption coefficient, which can be measured using THz-TDS [63]. In the pharmaceutical industry, it may be used to assess the coatings on tablets. It allows for the thickness and uniformity of the table to be measured, which impacts the tablet's shelf life-time and as well as how it is absorbed by the body. Minimal sample preparation is needed to test the tables using THz-TDS, and it may also be implemented on the production line, giving rapid results [65]. Packaged integrated circuits (IC) may be checked for quality using THz-TDS. Revealing the thickness of the hidden layers and the presence of any unwanted materials. Components may be authenticated by comparing the interior structures through THz imaging [66].

Many military aircraft use composite materials such as fiberglass, carbon fiber, and Kevlar due to their high strength. While these materials weaken over time, it is important to monitor them to ensure the aircraft's safety and continued high performance. The current inspection methods used are complicated, but THz-TDS can offer a rapid, no-contact inspection method to find defects as they develop [67]. In the aircraft and automotive industry, closely monitoring the thickness of protective coatings applied ensures functionality over its lifetime, while also reducing the money spent on the coating materials. Typically, many layers of coatings are used, and the only way to test the layers through destructive methods, such as wedge cutting. THz-TDS offers a solution by allowing for the thickness of each layer to measured non-destructively, and is already used by many in this industry [63]. Similar to how THz-TDS is used for quality control in many industries, the goal here is to use it to test the strength of CNT yarns, with the hope that it may be used in the production process for rapid testing.

2.2.1 Generation and Detection of THz pulses

There are a number of ways to generate and detect THz pulses, the most common approaches are: photoconductive antennas, optical rectification in a nonlinear medium, plasma ionization in air, and spintronic emitters. To detect THz pulses, common techniques include electro-optical sensing and photoconductive antennas [68]. In optical rectification, the laser pulse is focused onto a dielectric nonlinear crystal. The crystal material is instantaneous polarized, which generates the THz pulses. Different crystal materials affect the bandwidth of the generated pulses, and in some cases the field magnitude of the generated THz pulses will increase linearly with the thickness of the crystal material [69]. The phases of the incident optical radiation and generated pulse must be matched to ensure that they do not come out of phase as they propagate. Using a thinner crystal helps with phase matching, but results in less power in the emitted THz pulse [68].

Plasma ionization was first demonstrated in 1993 by Hamster et al. [70]. Femtosecond pulses are focused on an optical media, if the field as sufficient strength electrons will separation and ionization will occur. THz pulses radiate from this induced plasma. There are two different schemes for this technique: one-color field, where the optical pumping pulse has one central wavelength, and two-color field, where the pumping pulse has two central wavelengths. One-color field was the first to be demonstrated, but it cannot be used practically due to its lower conversion efficiency [71]. In two-color field, both pulses are focused by a lens or parabolic mirror into the media where the ionization occurs. The resulting THz pulse has a very smooth spectrum and exhibits characteristics ideal for THz spectroscopy [72]. THz generation from spintronic emitters utilizes spin current excitation and the inverse spin Hall effect. A multilayer structure made of ferromagnetic and nonmagnetic layers is pumped by a femtosecond laser pulse. The electrons in the ferromagnetic layer experience spin-dependent excitation, and these electrons are then diffused into the nonmagnetic layer. The inverse spin Hall effect occurs in this layer as the spin-current is converted into a charge current. A short THz pulse that propagates perpendicular to the current is generated as a result [73]. THz pulses generated this way have been shown to have a high amplitude using low pump power, as well as a large bandwidth without gaps. The bandwidth is similar to that of plasma system while being cheaper and easier to use [74].

This experiment uses InGaAs photoconductive antennas for THz generation and detection. Figure 11 shows a broadband THz pulse that we used in our measurements. It is a nearly single-cycle electromagnetic transient with a duration of several picoseconds and a corresponding bandwidth that extends up to 3 THz. Photoconductive antennas (PCA) for THz generation were first developed by Auston et al. in 1984 [75]. Due to the excellent performance, low cost, and relative straightforwardness of use, PCAs have become the most common and widely used as THz sources. The structure of a PCA consists of two DC biased metal dipole contacts, separated by a small distance, that have been fabricated onto a semiconductive material. The semiconductor is highly resistive, so no current will flow between the antenna contacts [76]. They are then optically pumped using an ultrashort pulse, commonly with a femtosecond duration. The wavelength of this pulse should be short enough so that the photon energy is greater than or equal to the band gap of the semiconductor[77]. When such pulse is incident on the gap between the antenna contacts, is absorbed and photocarriers are generated. The carriers are generated at a rate proportional to the incident optical pulse fluence[78]. The semiconductor experiences an instantaneous drop in resistivity as a result of the generated carriers, which are then accelerated in opposite directions by the DC bias field [79]. This produces a transient photocurrent, $J(t)$ that emits an electromagnetic pulse proportional to the time derivative of the current, $E(t) \propto \partial J(t)/\partial t$ [68]. The design and geometry of the PCA affects the emitted THz pulse,

but the most common design is the Hertzian dipole antenna [80]. The emitted pulse is then collimated by an attached lens, typically made of Si.

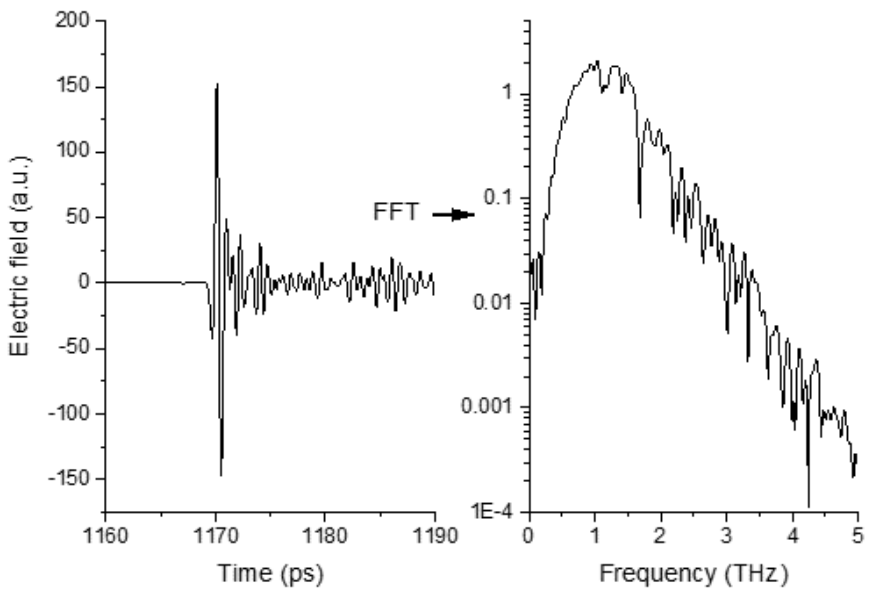

Figure 11: Signal that has been transformed to the frequency domain using a Fourier transform

PCAs used for detection are identical to the emitters, but without the voltage bias. When the laser pulse reaches the gap of detector PCA, photocarriers are generated, which rapidly changes the conductivity. The incoming THz pulse accelerates the photocarriers from one side of the antenna to the other, producing a measurable current in the gap. This current and its direction are proportional to magnitude and direction of absorbed THz pulse electric field, [68]. The laser pulse gates the detection of the THz pulse because its time duration is much narrower than that of the THz pulse. Varying the arrival time of the laser pulse allows reconstructing, point by point, the entire THz pulse waveform, since the current is only measured when the two pulses are simultaneously present at the detector [81]. The shape of the THz pulse depends on the duration of the optical pulse and carrier lifetime, shorter times being preferred for both [79].

Gallium arsenide (GaAs) is a common photoconductive material used for the PCA substrate. Its bandgap at room temperature is 1.42 eV (871 nm) [78], and it can be pumped using 800 nm (1.55 eV), making it compatible with titanium-dope sapphire lasers [79]. Low-temperature-grown GaAs (LT-GaAs) has a high concentration of point defects in its crystal lattice. Those defects introduce localized trap states for photoexcited free carriers, thus dramatically reducing the lifetime of carriers to less than one picosecond. If the carrier lifetime in the material is too long, the photocurrent pulse width to be broadened and result in a reduction in the THz pulse bandwidth [78]. To maximize the THz generation, the semiconductor material must have a short carrier lifetime and high carrier mobility [76]. The carrier lifetime of the antenna material also plays an important role in PCAs used for detection, as it affects the response function. Using materials with shorter-carrier lifetimes results in larger THz bandwidths because the temporal response in sharper. LT-GaAs is typically used because the carrier lifetime is about 100 to 300 fs [61].

2.2.2 THz-TDS Set Up

The main components of a THz-TDS system are a terahertz emitter and detector, an ultrafast laser, and a delay line[68]. Figure 12 shows a schematic for a general THz-TDS system. An ultrafast, femtosecond laser is used in the generation and detection of terahertz pulses. The ultrafast laser allows the system to have a high enough time resolution. The laser pulses are separated into two using a beam splitter, providing optical power to an emitter and receiver. One beam passes through a delay stage, typically the beam for the receiver. This allows for control over the arrival time by varying the length of the path of the laser travels. The THz field is measured only when the laser pulses are received at both the emitter and detector at the same time[61]. Varying the difference in arrival times of the pulse between the emitter and receiver using the delay stage allows for the electric field of the terahertz pulse to measured point by point, resulting in a time-domain measurement [68]. Parabolic mirrors focus the generated THz pulse onto a sample, once the THz pulse passes through the sample another set of parabolic mirrors recollimate the pulse to the detector. Reference measurements must be taken in order to gain useful information about the sample material.

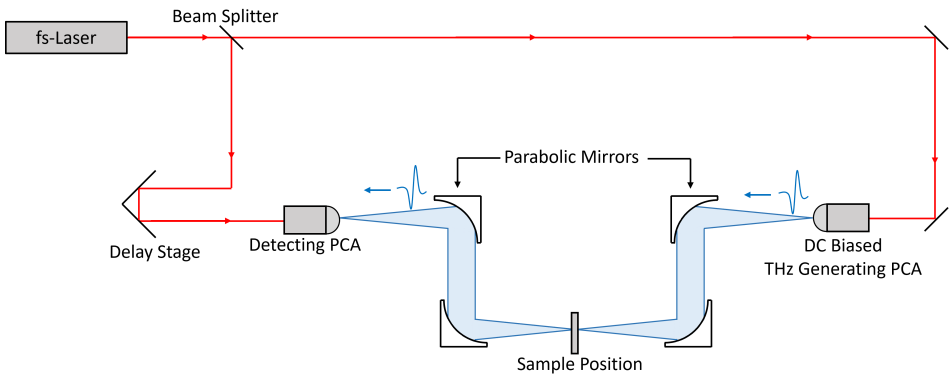

Figure 12: Schematic of a typical THz-TDS system

The pump beam can be modulated using an optical chopper to increase sensitivity and to achieve a high signal-to-noise ratio. The induced THz modulation is measured with a lock-in amplifier. The modulated frequency is used as the reference for the lock-in amplifier, so components that don't share the same frequency and a certain phase shift are not recorded [82]. THz-TDS relies on coherent detection methods, such as PCAs, for the measurement of the THz pulse in the time domain. The amplitude and phase of the THz pulse's spectral components can be analyzed by doing a Fourier transform. Comparing the spectral components of a reference pulse to that of the sample pulse allows for the calculator of the complex refractive index [61]. Many methods for retrieving the phase, absorption coefficient, and refractive index from THz-TDS measurements have been developed [83] [62].

The transmission and reflection of THz pulses can be analyzed using the Fresnel equations and the complex refractive indexes, $\tilde{n} = n + ik$ with n being the refractive index and k being the extinction coefficient. The Fresnel transmission and reflection coefficients for s and p polarization can be found below:

$$r_s = \frac{\tilde{n}_1 - \tilde{n}_2}{\tilde{n}_1 + \tilde{n}_2} \qquad r_p = \frac{\tilde{n}_2 - \tilde{n}_1}{\tilde{n}_2 + \tilde{n}_1}$$

$$t_s = \frac{2\tilde{n}_1}{\tilde{n}_1 + \tilde{n}_2} \qquad t_p = \frac{2\tilde{n}_1}{\tilde{n}_2 + \tilde{n}_1}$$

Using the Fresnel equations, analytic expressions for the calculations of the index of refraction and absorption coefficient can be found by considering transmission through a sample with thickness d. Relating the complex transmitted THz field, $\tilde{E}_t(\omega)$, with the complex field of the THz reference, $\tilde{E}_0(\omega)$:

$$\frac{\tilde{E}_t(\omega)}{\tilde{E}_0\omega} = T(\omega)e^{i\phi(\omega} = \tilde{t}_{12}\tilde{t}_{21}e^{i(n-1)\omega d/c} \tag{4}$$

This is done by inverting the Fresnel equations. Here, t_{ab} is the Fresnel transmission coefficient at the interfaces [72]. Using the Fresnel transmission equation, equation 4 can be written:

$$\frac{\tilde{E}_t(\omega)}{\tilde{E}_0\omega} = T(\omega)e^{i\phi(\omega} = \frac{4\tilde{n}}{(1+\tilde{n})^2}e^{1(\tilde{n}-1)\omega d/c} \tag{5}$$

In this equation, $(n-1)\frac{\omega d}{c} = \phi(\omega)$ is the spectral phase. It holds important information about the material's optical properties, like the refractive index [84].

$$n(\omega) = 1 + \frac{\phi(\omega)c}{\omega d} \tag{6}$$

Equation 6 shows how the refractive index may be found with the spectral phase. The absorption coefficient may be calculated as well, seen in Equation 7 [84] [72].

$$\alpha(\omega) = -\frac{2}{d}ln\left(\frac{(n+1)^2}{4n}T(\omega)\right) \tag{7}$$

3 Methodology

3.1 THz and CNTs

THz-TDS has been shown to be a powerful technique for characterization of CNTs. Previously, it has been used to study CNT thin film refractive index [85], MWCNT vibrations [86], and their electrical and optical characteristics.

Jeon et al. (2003) studied the dynamic response of CNTs in the THz range using THz-TDS. A thin film of CNTs was created and measured in parallel and perpendicular orientations, with respect to the THz beam polarization. The amplitude of the spectra varied with the orientation of the thin film, with the parallel orientation having a lower amplitude. Conductivity and index of refraction show dynamic changes over the 0.2 to 2.0 THz range. For both orientation, the conductivity increased with frequency until 0.45 THz, where it began to decrease. It was found that the index of refraction decreased with frequency, and power absorption increased with frequency, but it is theorized that both of these could also be affected by the density of the CNT film. The trends of these measurements are consistent over the two orientations, but the difference in magnitudes remains. This highlights the anisotropic behavior of the CNTs.

Additionaly Ren et al. (2009) investigated the use of thin films of highly aligned SWCNTs as a linear THz polarizer. The aligned CNTs exhibit high linear dichroism (LD) due to their anisotropic behavior. LD describes the difference in linerally polarized light absorption parallel and perpendicular to the orientation axis. Equation 8 shows how LD can be calculated using the parallel and perpendicular absorbance, $A_{\parallel}$ adnd $A_{\perp}$ respectively [87].

$$LD = A_{\parallel} - A_{\perp} \tag{8}$$

In the 2009 Ren et al. study, the reduced linear dichroism (LD^r) was used to measure the alignment of the films using their THz transmission data, as (LD^r)) is not affect by film thickness. It can be expressed with:

$$LD^r = 3((3cos^2\alpha - 1)/2) * S \tag{9}$$

α is the angle between dipole moment direction and the long axis, and S is the nematic order parameter. S = 1 would describe perfectly aligned CNTs, and S = 0 would mean the CNTs are randomly oriented. The films created by Ren et al. had a nearly constant LD^r of 3, meaning that $S \sim 1$ and the CNTs were well aligned. The films were shown to be excellent polarizers in the THz region, the high angular dependence can be seen in figure 13. When the film was parallel to the THz filed,$\theta = 90°$, absorbance was high and increased with frequency. The absorbance decreases as the angle θ was increased from 0° to 90°. In the perpendicular orientation, $\theta = 90°$, the absorbance was zero across the frequency range.

In 2012, Ren at al. also demonstrated a THz polarizer using stacks of CNT films. In both 2009 and 2012, Ren et al. characterized the effectiveness of their CNT polarizers by calculating the degree of polarization (DOP). It was found by first calculating the transmittance, T, of the film

$$T = |\frac{E_s}{E_r}|^2 \tag{10}$$

Where E_s and E_r are the electric field amplitudes of the frequency domain through the sample and a

reference measurement respectively. This is used to find the absorbance, A

$$A = -log_{10}(T) \tag{11}$$

The Degree of Polarization (DOP) of the aligned films was found using

$$DOP = \frac{(A_\perp - A_\parallel)}{(A_\perp + A_\parallel)} \tag{12}$$

Where $A_\perp$ is the transmittance when THz is perpendicular to CNT film alignment axis, and $A_\parallel$ is transmittance when parallel[88]. The DOP for the created CNT THz polarizer reached a value of 99.9%, showing the film acts as a near perfect polarizer [89]. The DOP can also be used to quantify the alignment of CNTs, as higher alignment means higher DOP due to the anisotropic behavior. This behavior is preserved even in self-assembled bundles of CNTs, meaning that measuring the DOP of a bundle could lead to insights about the alignment of the tubes within [88].

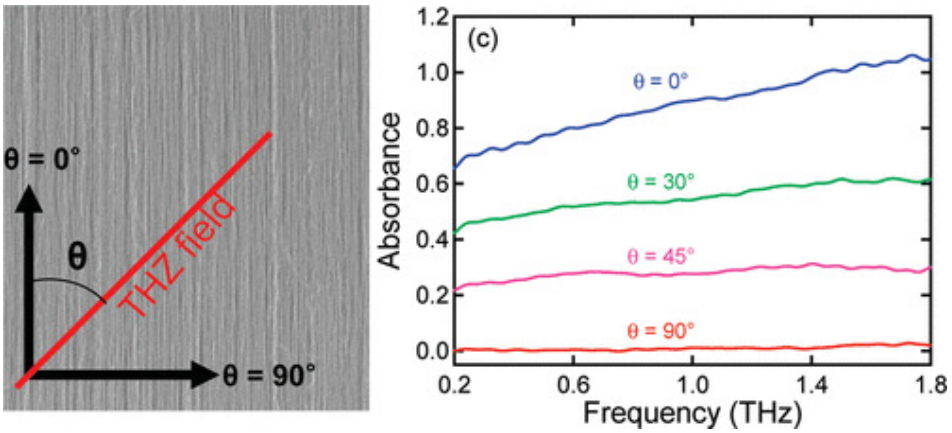

Figure 13: On the left, SEM image of highly aligned CNT film with diagram of THz field orientation On the left, THz absorbance spectra for the film at different polarization angles. Reprinted with permission from [88]. Copyright 2009, American Chemical Society.

3.2 Experimental Method

Miralon® CNT yarns were studied, with samples provided by Nanocomp Technologies, Inc., a subsidiary of Huntsman Corporation. Two yarns with different tensile strengths were compared. Before measurements were taken, the sample was mounted on a quartz slide, which can be seen in figure 14. The yarn was doubled back on itself so that multiple sections of the same yarn were parallel to each other. As the average width of the yarn is $10\mu m$, this method of placing yarns side by side is to make the width of test section of the yarn closer to 2mm, the diameter of the beam spot of the THz pulse used. An optical microscope was used to ensure that the yarns were truly parallel to each other with minimal gaps between. This can be seen in Figure 15, an image take with the microscope of four yarn sections mounted side by side, so a width of 1.8 mm was achieved.

The TeraFlash pro system from TOPTICA was used to make the THz-TDS measurements. Figure 16 shows a schematic of this specific system, with the red lines representing optical signals. This system makes use of InGaAs PCAs for THz pulse generation and detection, and has a spectral range of 0.1 to 6 THz. The laser providing optical power has an 80 fs pulse width and a 1560 nm (0.8 eV) wavelength. This wavelength is suitable for the excitation of the InGaAs, as it has band gap is 0.75

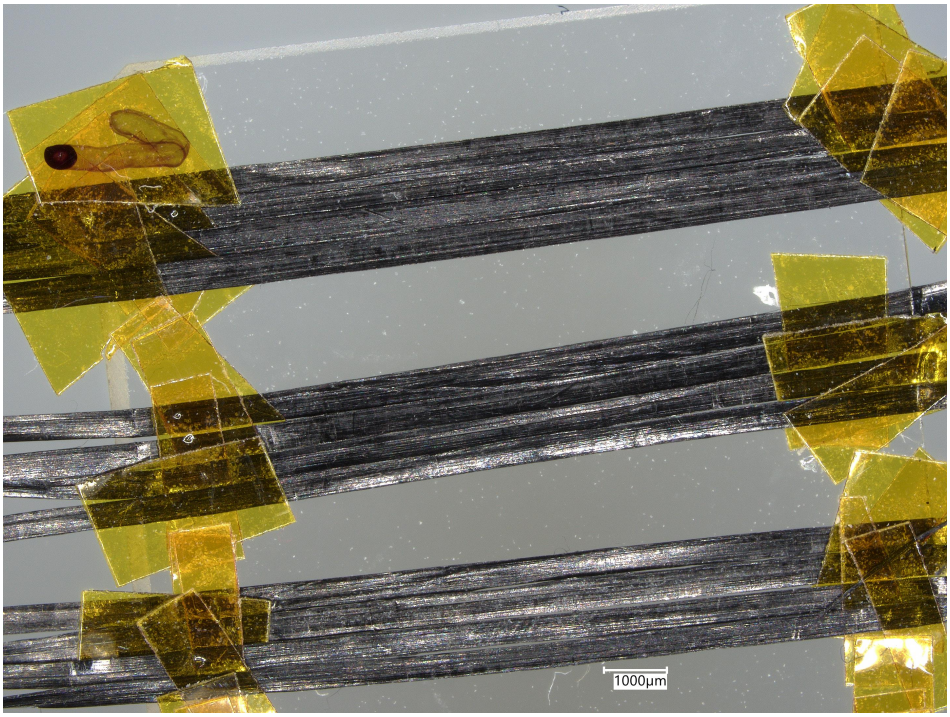

Figure 14: Microscope image of CNT yarn. Four sections of the same yarn have been double backed, so they are side by side. The total width of the section is approximately 1.8 mm

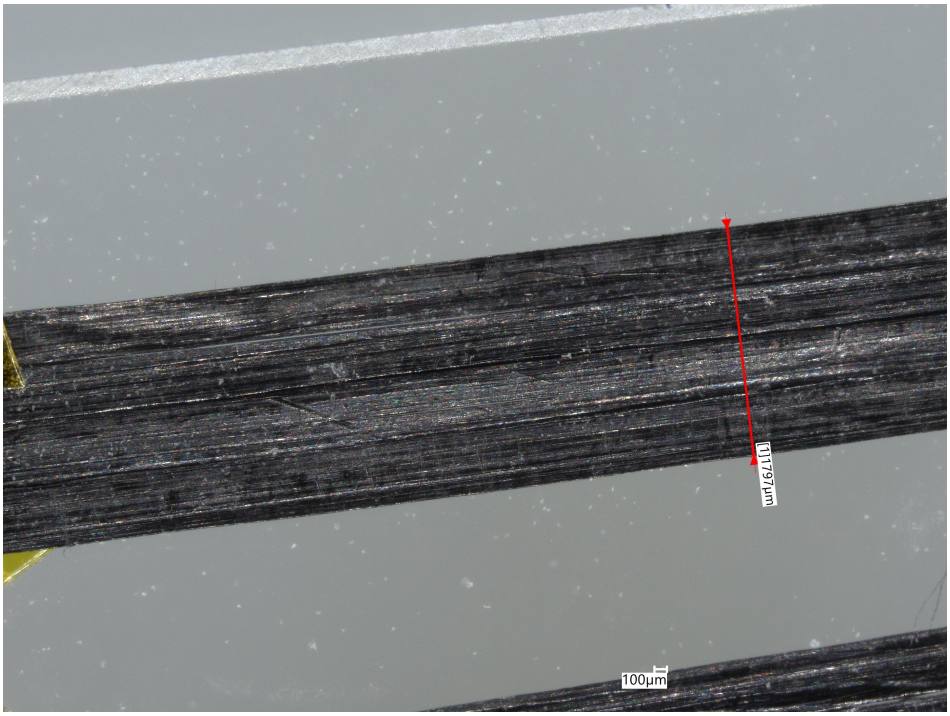

Figure 15: Microscope image of CNT yarn. Four sections of the same yarn have been double backed, so they are side by side. The total width of the section is approximately 1.8 mm

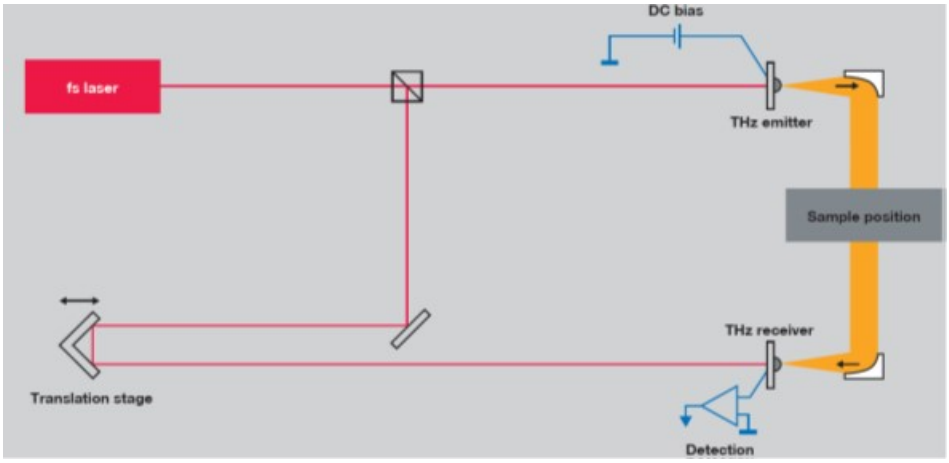

Figure 16: Schematic of the TOPTICA TeraFlash pro [92]

eV at room temperature [90]. Using 1560 nm for the excitation of InGaAs allows for the system to make use of components previously designed for telecommunications [91]. Optical fibers guide the laser beam to the PCAs, allowing for a flexible set-up. A rotation stage is added to set up so the absorption of the CNT yarn may be tested at different orientations with respect to the direction of the THz pulse polarization. Figure 17 shows the experimental set-up that was used. The rotation stage may be seen on the metal plate under the detecting PCA. As the CNT yarn is rotated 360°, the magnitude of the electric field will change as more or less of the THz pulse is absorbed. The rotation stage is also fitted with a 2 mm diameter aperture, that yarn is placed over. The aperture is centered over the THz focus spot. The centering may be checked using the TeraFlash imaging software and checking the change in the measured pulse through a full rotation. If the aperture is not centered, the magnitude of the THz pulse will change with the rotation from the stage covering part of the beam, preventing an accurate measurement of the sample.

The first measurements taken are a reference measurement, which is done through the quartz slide with no sample present. This measurement is used when comparing measurements through the sample and is retaken often as changes in lab conditions, like humidity, affects the THz pulses. After this, the sample is placed on the rotation stage and measurements are taken through a full rotation, in 15° steps. The full rotation is done so the parallel and perpendicular orientations of the yarns may be found. Figure 18 shows a comparison of the THz pulse passing through air and the CNT yarn sample when parallel and perpendicular.

A rotation stage is added to the setup in order to find the DOP of CNT yarns. As the CNT yarn is rotated 360°, the magnitude of the electric field will change as more or less of the THz pulse is absorbed. By comparing the change in absorbance over the full rotation, the points where the alignment axis is parallel and perpendicular to the THz polarization can be found. Small steps in the rotation allows for small changes in the absorption to be measured. The $A_{\perp}$ orientations occur where the absorption reaches the minimum and $A_{\parallel}$ occurs at the peak of absorbance. The DOP can then be found using equation 12.

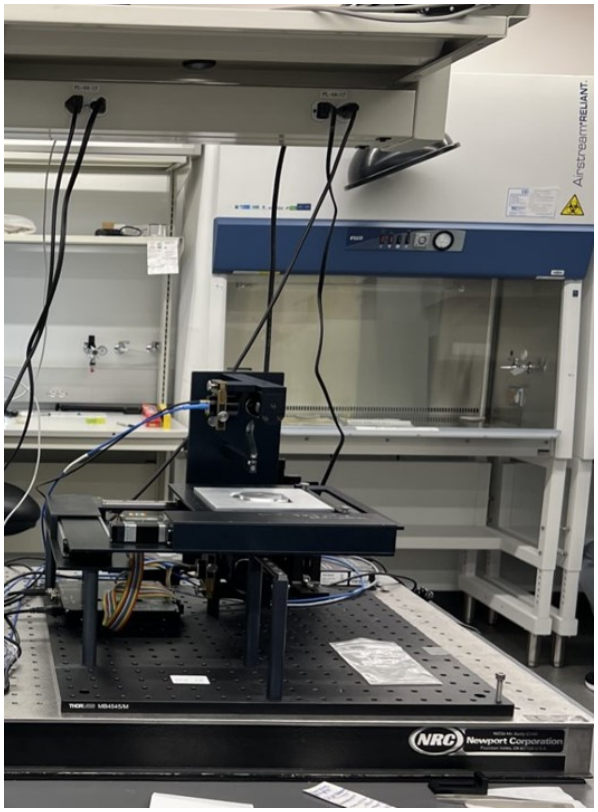

Figure 17: Photo of TeraFlash Pro system used. The sample was placed on the rotation stage.

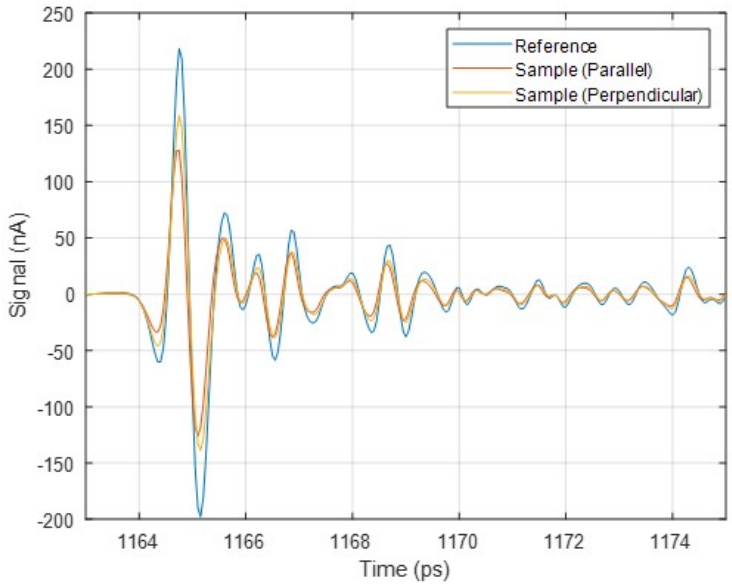

Figure 18: Comparison of the THz pulse through air and CNT sample when parallel and perpendicular. Signal magnitude decreases when passing through the sample, and further decreases depending on the sample orientation

3.3 Data Analysis

A Fourier transform is done to transform the electric field waveform from the time domain to the frequency domain. To accomplish this, a Fast Fourier transform (FFT) was used, which is a computer algorithm that calculates the discrete Fourier transform. Using the frequency domain of the THz pulse, the absorbance of the sample is calculated by comparing the electric field amplitudes of the electric field data. The absorbance was found in the same manner that was done by Ren et al. in 2012, with transmittance being calculated first in the following way:

$$T = |\frac{E_s}{E_r}|^2 \tag{13}$$

Rather than using the electric field amplitudes for E_s and E_r, the transmittance was found over the whole frequency domain, so comparisons of the whole spectrum may be done later. Using the transmittance found over the whole domain in equation 14 results in the absorbance across the domain as well.

$$A = -log_{10}(T) \tag{14}$$

Once the absorbance of the yarn in the parallel and perpendicular orientations are known, the DOP is calculated. Since a full rotation of the sample was done, the orientations can be found but comparing the magnitude of absorbance to the angle of the sample. For this comparison, the magnitude of absorbance was found with the area under the absorbance spectrum curve. Plotted compared to the angle, which can be seen in figure 19, the absorbance magnitude forms a sine curve as the absorption changes through the rotation. Here, $A_\perp$ occurs when the absorbance reaches a minimum, and $A_\parallel$ occurs when the absorbance reaches. Each orientation occurs twice due to the 360° rotation. A sine fit to this curve was used to find the "average" absorbance for the two orientations, parallel and perpendicular. The amplitude values from the sine fit were used as $A_\perp$ and $A_\parallel$ in equation 15 to find the DOP for the sample.

$$DOP = \frac{(A_\perp - A_\parallel)}{(A_\perp + A_\parallel)} \tag{15}$$

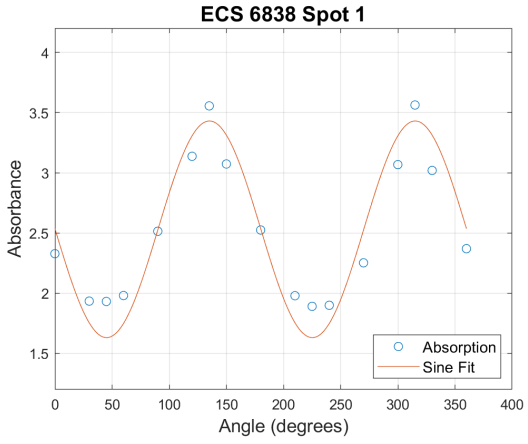

Figure 19: Absorbance of the sample plotted against angle with its sine fit

4 Results and Discussions

	Tex (g/m)	Tenacity (N/Tex)
Yarn 1	9.2	1.4
Yarn 2	11.4	2.0

Table 1: Provided yarn tenacity data

The provided tenacity data from Nanocomp Technologies, Inc. can be seen in table 1. The tenacity of the yarn is described using N/Tex, with Tex being the linear density. The tenacity of yarn 1 is 1.4 N/Tex, while the tenacity for yarn 2 is 2.0 N/Tex. Based on this tenacity data, yarn 2 is the stronger of the two yarns. Images of the yarns using a scanning electron microscope (SEM) were also provided by Nanocomp, and can be seen in figure 20 and figure 21. The first image in both sets is on the 1 μm scale, and the second has a 500 μm scale. Bundles of CNT may be seen, not individual tubes. The bundles have many overlapping spots, and while they are not perfectly aligned, the bundles generally point in the same direction. Comparing the SEM images for the two yarns, their alignment appears similar and there is little difference to be seen between them.

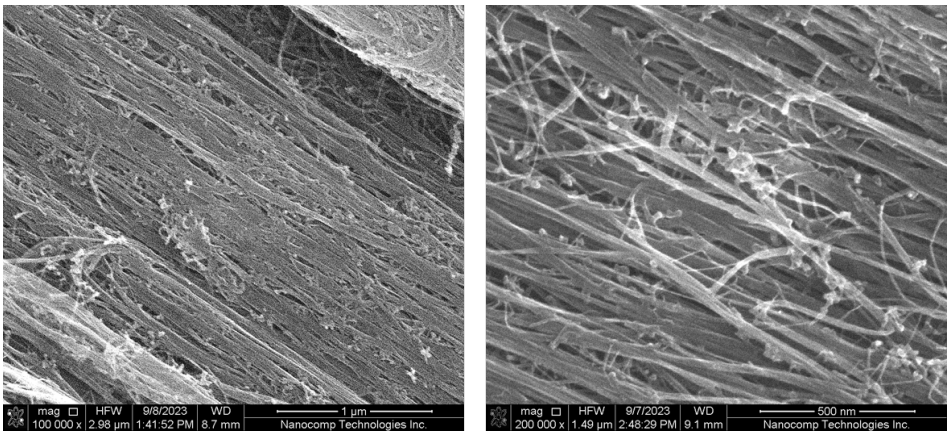

Figure 20: Provided SEM images for Yarn 1

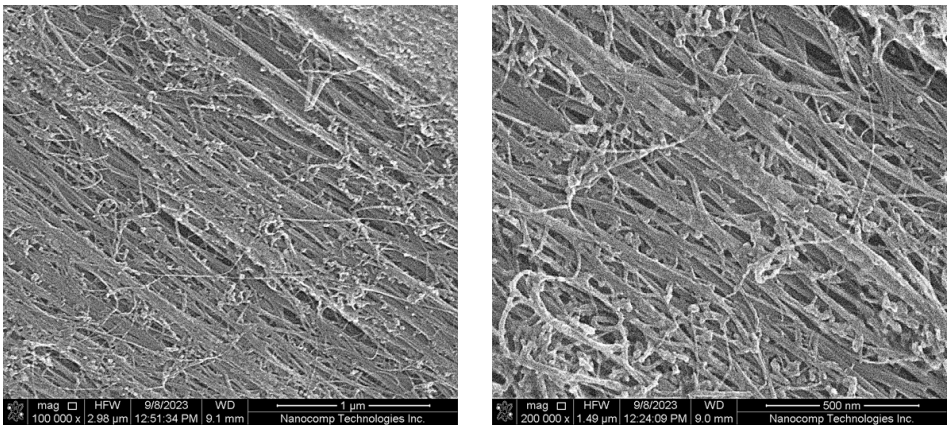

Figure 21: Provided SEM images for Yarn 2

The calculated DOP was used for further comparisons between the yarns. Four sections on each yarn, about 50cm apart, were tested. Both absorbance values were averaged for each section that was measured to produce a singular DOP value. Looking at yarn 1, the "weaker" yarn, the measured absorbance can be seen in figure 22, along with the calculated DOP for each spot. The DOP shows high variation from spot to spot, ranging from 21% to 47%. This shows that the alignment is not uniform along the yarn. The absorbance and DOP for yarn 2 are shown in figure 23. The DOP for yarn 2 ranges from 27% up to 42%. Like yarn 1, yarn 2 also shows high variation from spot to spot, showing the non-uniform CNT alignment within the yarn.

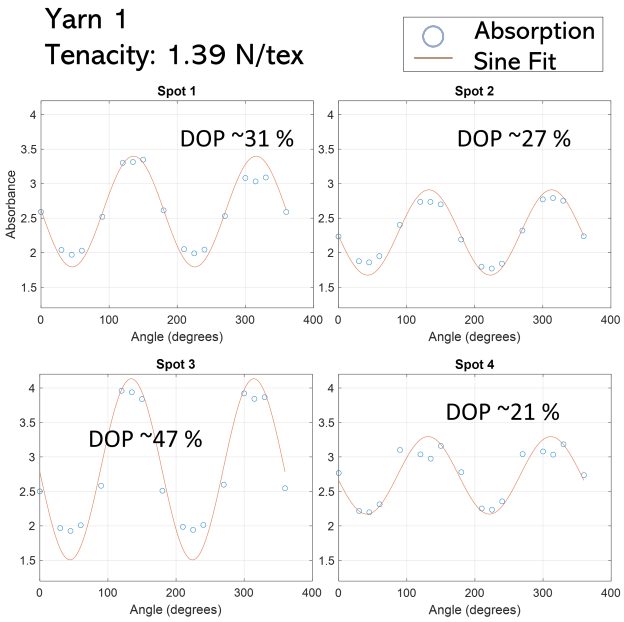

Figure 22: Sine fits and DOP for yarn 1 over 4 spots.

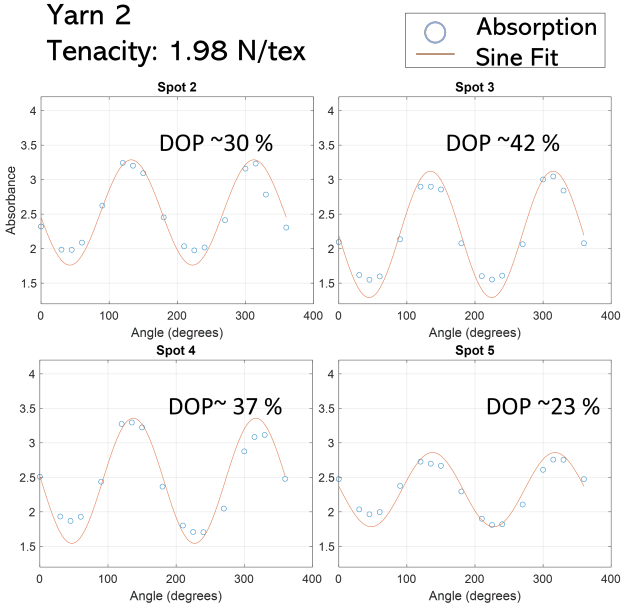

Figure 23: Sine fits and DOP for yarn 2.

While it was anticipated to use the DOP to compare the strength between the two yarns, with the stronger yarn having a higher DOP, no difference can be seen between the two yarns when using the DOP as a comparison point. The average percentage for both is similar, $32 \pm 11\%$ for yarn 1 and $33 \pm 8\%$ for yarn 2. Both yarns also show similar peak polarization values, rather than one showing a higher value compared to the other. The measured polarization percentages for the yarns are also low compared to the results in Ren et al. (2012), where the DOP for the film of SWCNTs was found to be close to 100%. The lower DOP may be a result of the residual materials left in the yarn from the manufacturing process. Leftover materials within the yarn, like amorphous carbon or graphite substrate, would not show anisotropic behavior, resulting in a lower DOP compared to a material of pure, aligned CNTs. Evidence of this may also be seen in the frequency amplitudes of the spots. Figure 24 shows the frequency spectrum for a single spot for the parallel and perpendicular orientations. While there is strong attenuation in both directions, there is still a significant amount of absorption in the perpendicular orientation, which suggests the presence of isotropic leftover materials.

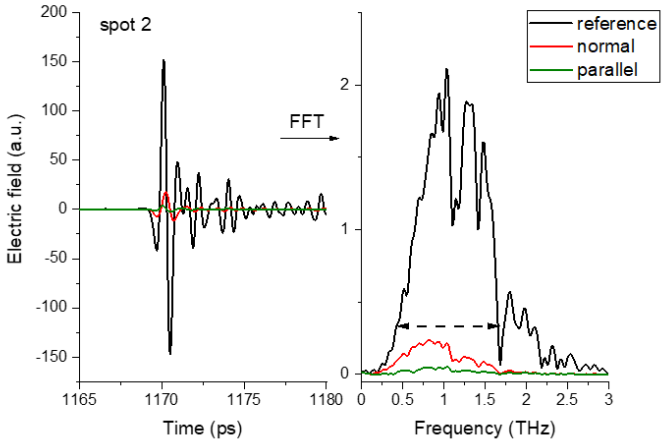

Figure 24: On the left, THz waveform for normal and perpendicular orientations. On the right, the corresponding THz amplitudes after a FFT

The absorbance spectra for the yarns were also investigated for differences. Looking at the absorbance spectra for yarn 1, in figure 25, there is high variation in the parallel absorbance between each spot. The spot with the highest DOP, spot 3, also shows the highest parallel absorbance spectrum. The spectra for yarn 2, figure 26, displays the high variation that was seen when comparing DOP as well. As with the DOP, there is no significant difference found between the two yarns when comparing their absorbance spectra. Comparing all the spots across the yarns, there is little change in their perpendicular absorbance, $A_{\perp}$. This is due to the residual, non-CNT, materials within in the yarn. As mentioned before, their non-anisotropic behavior causes the spots to have the same base absorbance.

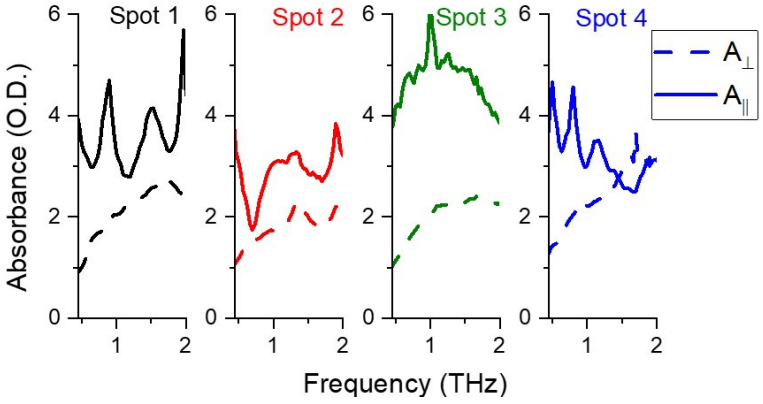

Figure 25: Absorbance spectrum for parallel and perpendicular orientations for yarn 1.

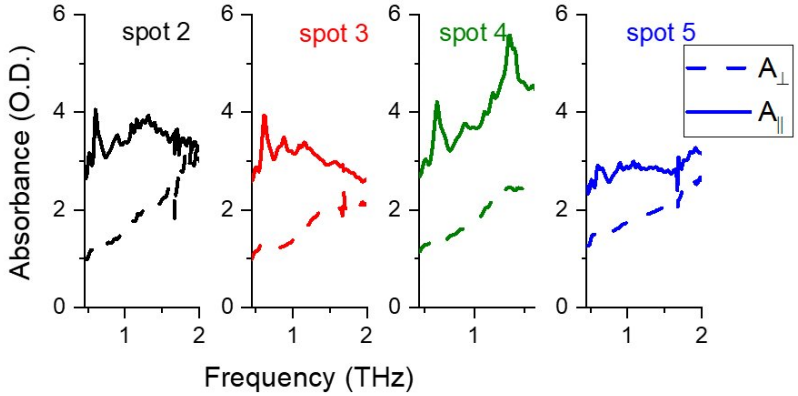

Figure 26: Absorbance spectrum for parallel and perpendicular orientations for yarn 2.

Differences between the yarns are found in their polarization spectra. This compares the polarization, found with 12, across the whole spectra of wavelengths rather than using the average to find a single value. Figure 27 shows the polarization for all four spots from 0.5 to 2 THz. Each spot shows its own peaks and valleys in the spectrum, and there is a high amount of variation between the spectra. The spot that had the highest DOP, spot 3, also shows higher polarization values across the whole spectrum compared to the other spots on the same yarn. The polarization spectra for the spots on yarn 2 are shown in 28. These spots share similar peaks along the spectra, and despite the variation in the DOP values, the polarization values show less variation. The spectra for yarn 2 shows more uniformity across the length of the yarn.

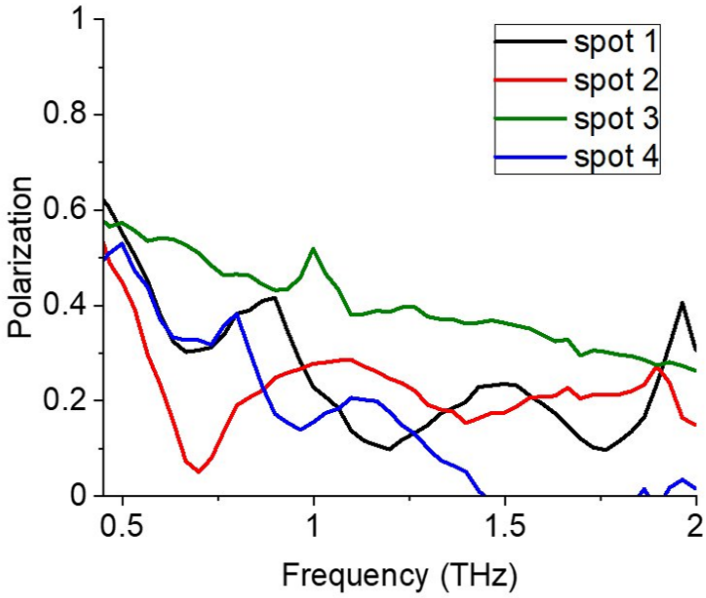

Figure 27: Polarization spectrum for yarn 1.

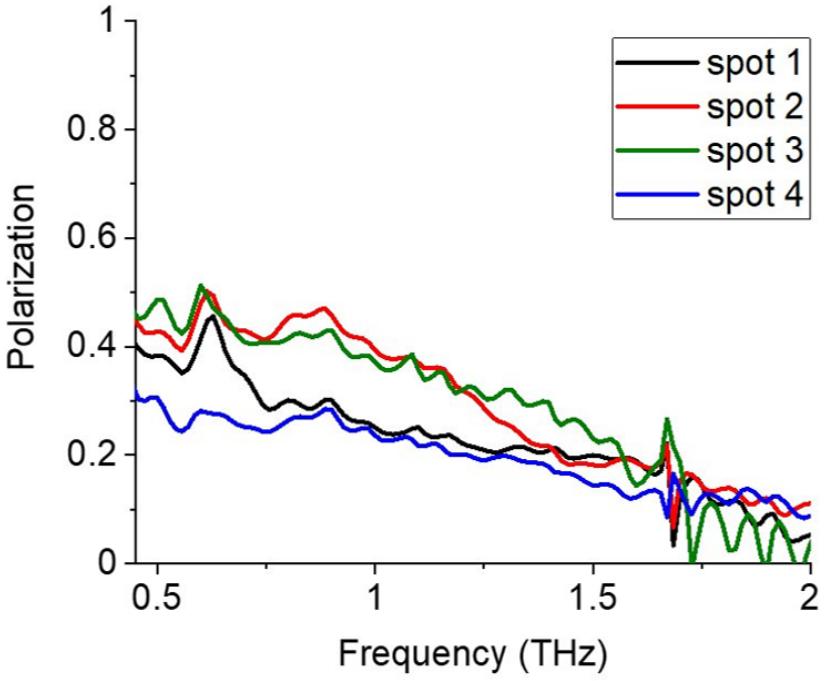

Figure 28: Polarization spectrum for yarn 2.

Measuring the alignment of CNTs within the yarn using the DOP doesn't allow for an assessment of the yarn's strength. This is due to the unique mechanical failure modes that are seen in CNT yarns. Downes et al. (2015) investigated the load transfer and failure modes of CNT sheets that were provided by Nanocomp Technologies, Inc. It was found that the CNTs self-assemble into bundles, with the possibility that CNTs with higher diameters may collapse, leading to more surface area. These collapses bundles of aligned CNTs still experience the tube pull-out, or "telescoping", failure mode despite their increased strength. Yarn failure even when the CNT alignment is increased in these bundles makes the strength more difficult to predict.

Rather than single spot alignment measurements, the uniformity of the polarization spectra maybe be used as strength assessment. As mentioned in the polarization spectra comparison, the spectra for the yarn 2 spots shows more uniformity than yarn 1. The lower variation in the spectra correlates to the higher tenacity yarn. Higher CNT alignment does lead to a higher strength in a single spot. The improved alignment of the CNTs within the yarn is what results in an increase of strength due to van der Waals force, but uniformity is what leads to the increased yarn tenacity, as the yarn is only as strong as its weakest point.

5 Conclusion and Future work

The feasibility of using THz-TDS to monitor the tensile strength of commercially produced CNT yarns was tested. Based on previous experiments that have been done, it was anticipated that the CNT yarn would act as a polarizer for the THz region and the degree of polarization would vary with the alignment of CNTs within the yarn. This would be used to predict the strength of the yarn based on an increase of alignment of individual CNTs within the yarn increasing the van der Waals forces holding them together, therefore leading to an increase in strength. CNT yarn samples were tested at multiple angles to find the degree of polarization in multiple spots.

When comparing two yarns of different strengths, it was found that the degree of polarization is not a predictor of strength. Instead, the stronger yarn showed more uniformity in its polarization spectra. This indicates that THz-TDS may be used to assess the strength of the CNT yarns. For future work on this project, additional spots on the yarn and on different yarn samples should be analyzed. Further investigation may reveal more trends in the yarns that can be used to characterize, or even predict, the strength of the yarn. Additionally, a THz-TDS system may be implemented into the Miralon® production process, an idea that is shown in figure 29. Two sets of THz emitter and receivers may test the yarn at the parallel and perpendicular orientations as the yarn is pulled through to test the yarn as it is being made.

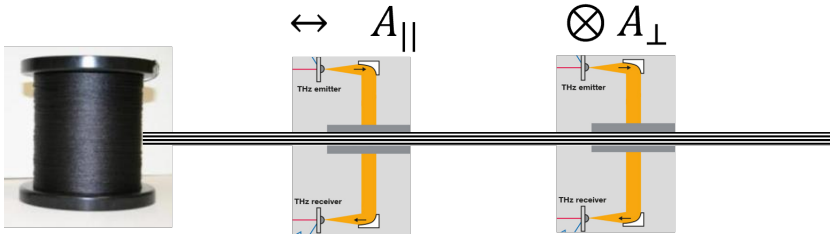

Figure 29: Idea for how two sets of THz emitters and receivers may be used to measure the absorbance of the yarn as it is being created.

6 Appendix

6.1 Toptica Operation Instructions

The Toptica TeraFlash Pro system is operated using the TeraFlash Control application, shown in figure fig. 30. To begin THz generation, the red switch on the system must be turned on, as well as the "Laser" and "RUN" switch within the application. After turning them on, it's best to wait at least 15 minutes for the system to stabilize.

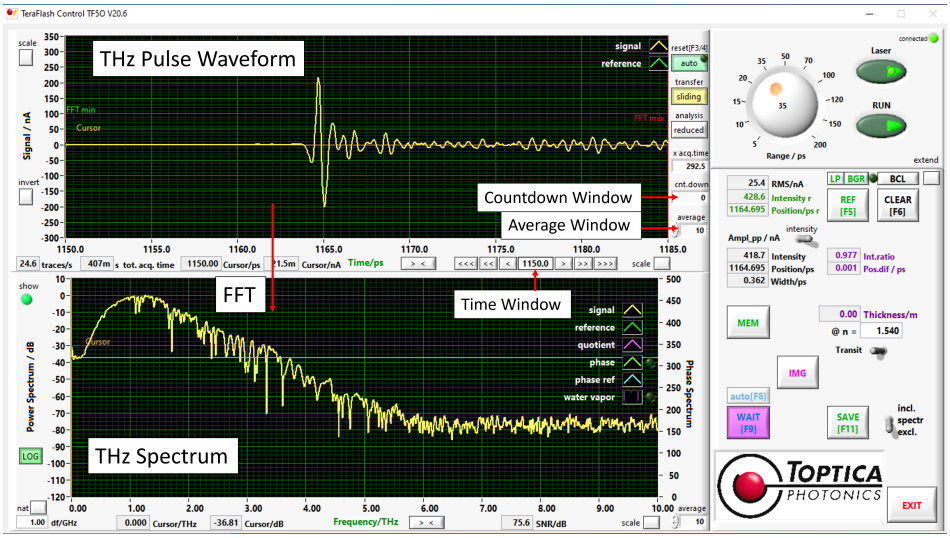

Figure 30: TeraFlash Control Application

The THz pulse waveform is displayed in the top left screen, and the spectrum for the pulse after an FFT is shown on the bottom. If the pulse is not seen in the top window, the time window may be adjusted using the box below the graph, it should be set to around 1150 ps. The intensity of the pulse is shown on the left middle of the screen. Adjusting the position of the PCAs or the stage.

The amount of averages per each measurement can be adjusted using the "average" box to the left of the waveform window. A higher number results in less noise in the measurement. Once the average is set, a count-down will the start in the "cnt. down" box above. Once the countdown is complete, the measurements will pause, and they can be saved using the "SAVE" button. The measurements may be unpaused using the "WAIT" button. Once unpaused, the "auto" button above will begin the countdown again.

The imaging extension can be accessed using the "IMG" button, and can be seen in figure 31. The windows under "X /mm" and "Y /mm" are used to set the staring position of the scan. The "DX /mm" and "DY /mm" sets the total size of the scan, while "dX /mm" and "dY /mm" adjust the sizes of the steps taking during the scan. The scan will begin after selecting "START", and the resulting image will be displayed. Imaging is useful for centering the aperture of the rotation stage over the THz beam spot. The X and Y values of the center p of the aperture may be found by looking at its image. Setting these values in the X and Y position boxes and selecting "Go Start" will adjust the position of the stage to those values.

The Picomotor Application is used to control the rotation stage, as seen in figure 32. The right and left arrows are used to rotate the stage clockwise and counterclockwise. Selecting "Jog (Free Run) allows for continuous rotation when clicking the right and left arrows. "Relative" mode will cause the motor to rotate a certain amount of steps when the clicking the arrows The amount of the steps

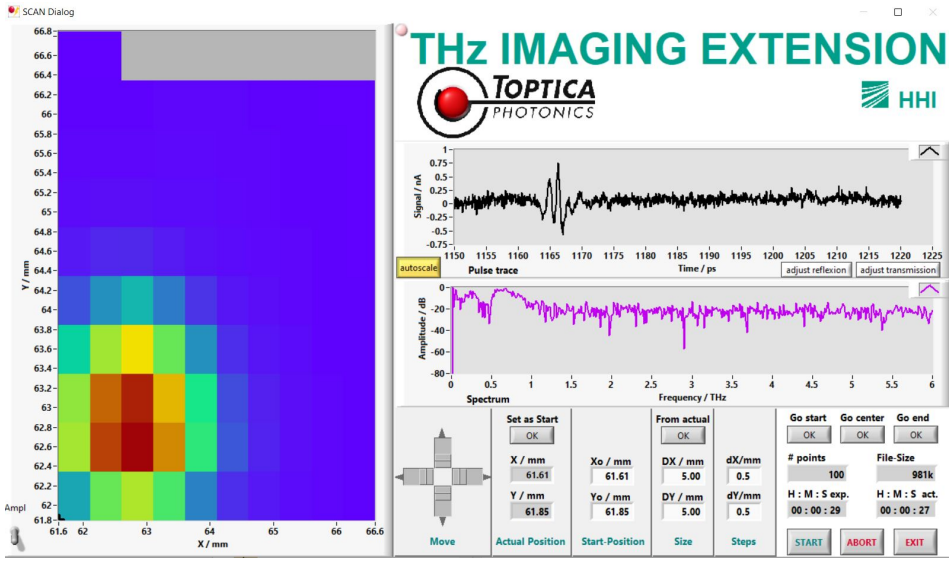

Figure 31: Toptica Imaging Extension

may be adjusted in the "Relative Steps" window above the arrows It is helpful to do a full rotation of the stage while monitoring the displayed intensity in the TeraFlash Control application to get an idea of the alignment. When the aperture on the rotation stage is not properly aligned, there will be significant changes in the intensity as it cuts the beam.

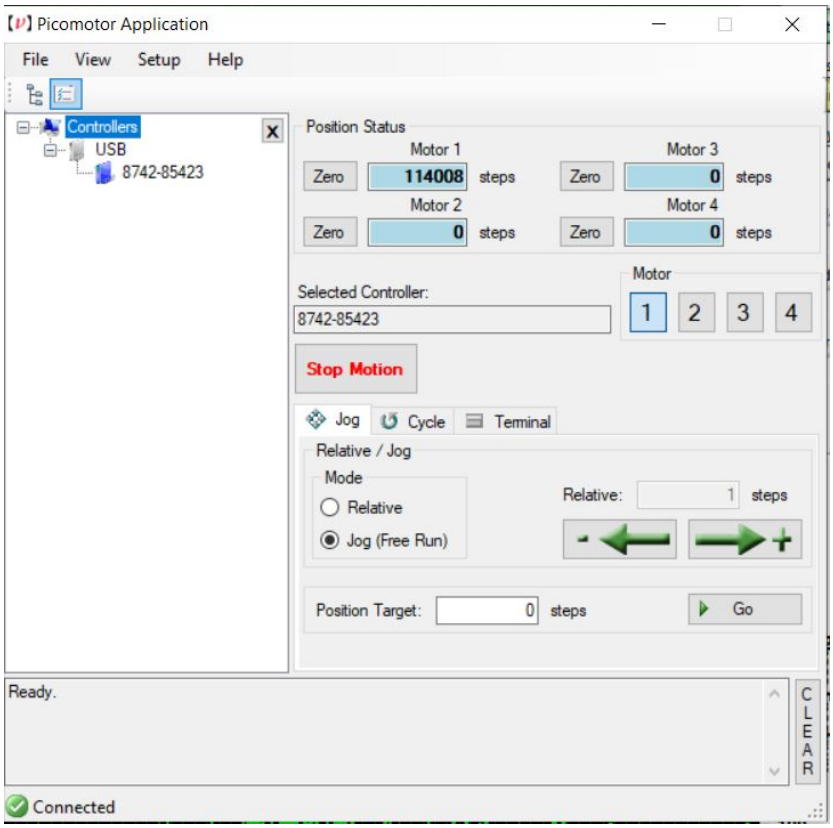

Figure 32: Toptica Imaging Extension

6.2 Code Used for Data Analysis

See following page. Code made using MATLAB R2023a.

Files

Copy and paste name of the folders for the reference and sample data.

Here, the code assigns each file a number based on angle ascending angle (0° is 1, 30° is 2, 60° is 3....). This is only used when you want to plot specific angles

```
clear all;
reffolder='Reference Quartz 8 30 2023';
sampfolder='ECS 6838 Quartz 5 8 30 2023';
name = 'Spot 5';

reffiles=dir([reffolder '\*.csv']);
numfiles=length(reffiles);

clear ref samp
for m=numfiles:-1:1
    temp=readmatrix([reffolder '\' reffiles(m).name]);
    ref(m).time=temp(:,1);
    ref(m).data=temp(:,2);
    temp=readmatrix([sampfolder '\' reffiles(m).name]);
    samp(m).time=temp(:,1);
    samp(m).data=temp(:,2);
    temp=strfind(reffiles(m).name,'.');
    angle(m)=str2double(reffiles(m).name(1:temp(1)-1));
end
numsamples=size(samp(1).data,1);
[angle,index]=sort(angle);
ref=ref(index);
samp=samp(index);
```

FFTs

```
numfreq=ceil(numsamples/2);
sampfft=zeros(numfiles,numfreq);
reffft=zeros(numfiles,numfreq);
for m=1:numfiles
    temp=abs(fft(samp(m).data));
    sampfft(m,:)=temp(1:numfreq);
    temp=abs(fft(ref(m).data));
    reffft(m,:)=temp(1:numfreq);
end
maxfreq=1/.05e-12/2;
freq=maxfreq*(1:numfreq)/numfreq;
```

Plot FFTs

If you want to change what angles you are plotting, change the values in the index (line 40)

```
index = ([9 4]);
for m=index
```

```
    plot(freq/1e12,sampfft(m,:))
    hold on
end
xlim([0 3.5])
plot(freq/1e12,reffft(9,:))
hold off
grid on
xlabel('Frequency (THz)')
ylabel('Amplitude')
legend('Reference','Parallel','Perpendicular')
```

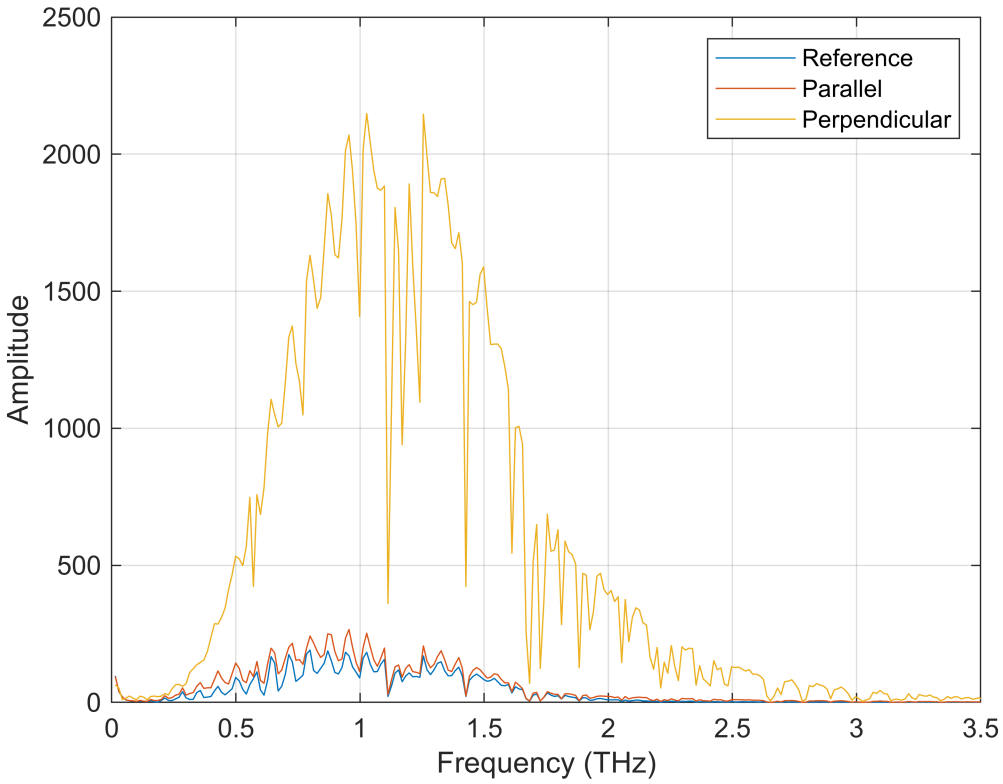

Sample Singal Max vs. Angle

```
sampmax=zeros(1,numfiles);
for m=1:numfiles
    sampmax(m) = max(samp(m).data);
end
plot(angle,sampmax)
grid
xlabel('Angle (Degrees)')
ylabel('Signal Amplitude')
title('Sample Signal Magnitude')
```

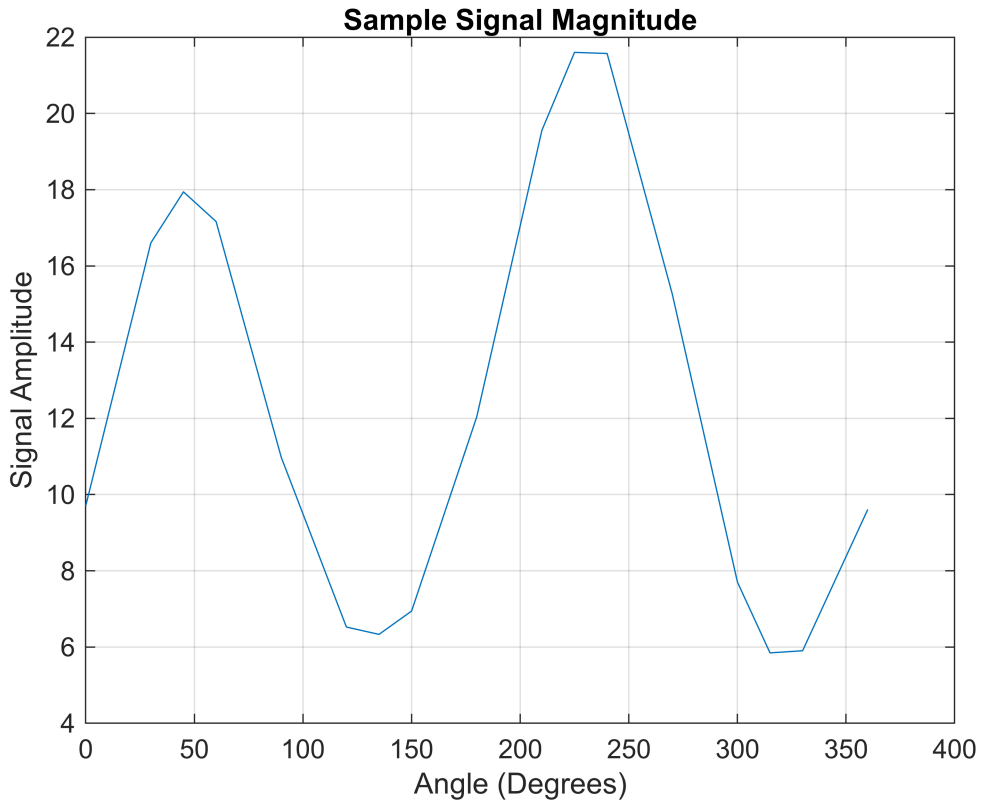

Absorbance vs. Angle

```
absp=zeros(1,numfiles);
for m=1:numfiles
    intsamp(m,:)=trapz(sampfft(m,:));
    intref(m,:)=trapz(reffft(m,:));
    temp=intsamp(m,:)./intref(m,:);
    absp(m)=abs(-log10((mean(temp))^2));
end
plot(angle,absp)
grid
title('Absorbance as a Function of Angle')
xlabel('Angle (degrees)')
ylabel('Absorbance')
```

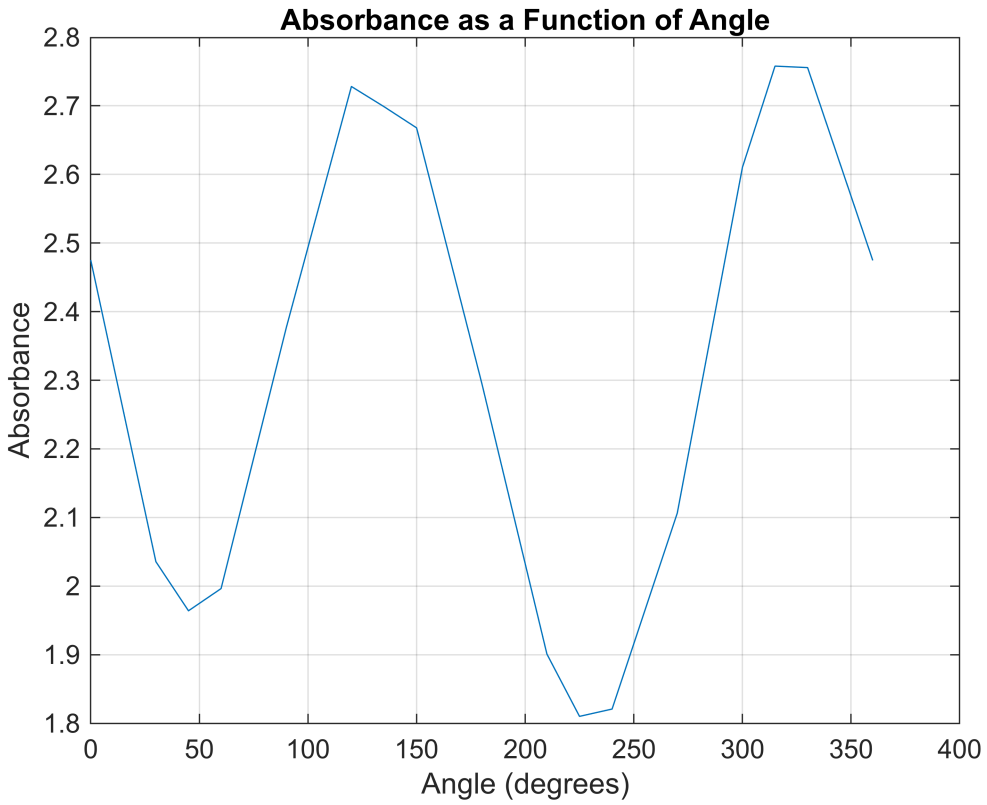


```
[fit,amplitude,~,offset,error] = fitsine(absp, angle);

plot(angle,absp,'o',fit.angle,fit.data)
grid
title('ECS 6862 Spot 3')
legend('Absorption','Sine Fit','Location','best')
xlabel('Angle (degrees)')
ylabel('Absorbance')
```

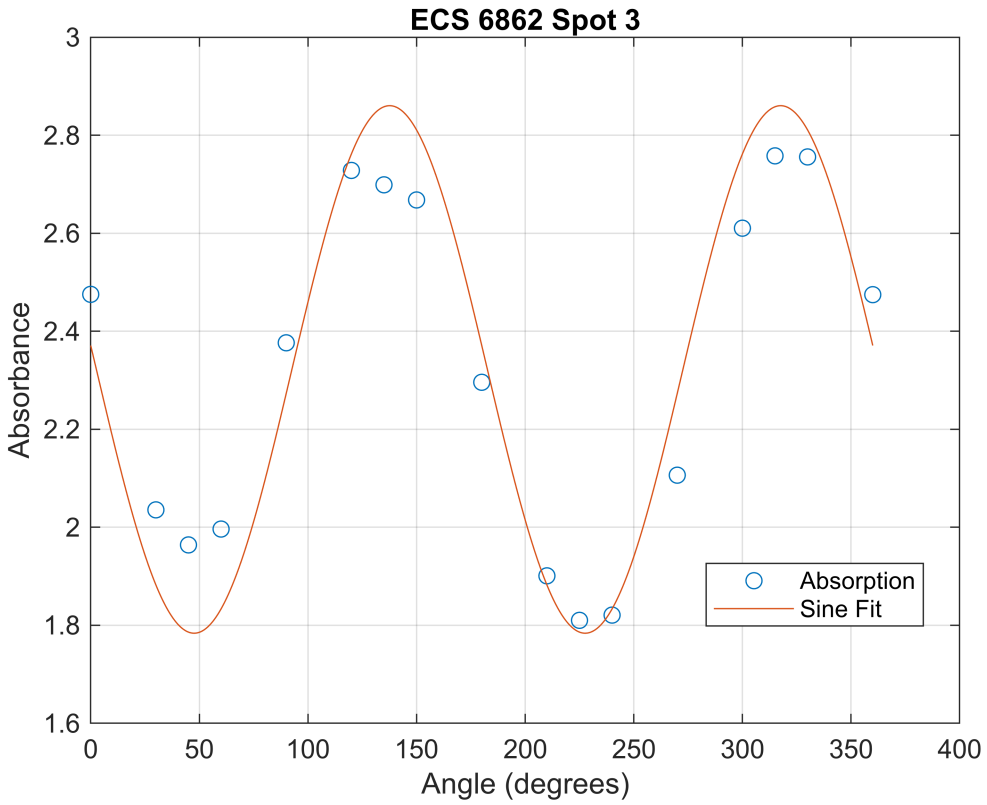

Average Absorbance and Polarization

```
%perpendicular polarization:
abspperp = offset - amplitude
```

```
abspperp = 1.7838
```

```
%parallel polarization:
absppara = offset + amplitude
```

```
absppara = 2.8602
```

```
%degree of polarization:
polarization = ((absppara - abspperp)/(absppara + abspperp))*100
```

```
polarization = 23.1782
```

Absorbance vs. Frequency Plot

If you want to change what angles are plotted, change the numbers in the index (line 91)

```
figure
hold on
abspentire=zeros(numfiles, numfreq);
%calculate aboorbance across entire spectrum:
for m=1:numfiles
    abspentire(m,:)=-log10((sampfft(m,:)./refffft(m,:)).^2);
```

```
end
index= ([3 6 9 11]);
for m = index
    plot(freq/1e12,abspentire(m,:))
end
hold off
legend(num2str(angle(index)'),'Location','eastoutside')
xlim([0.5 2.5])
xlabel('Frequency (THz)')
ylabel('Absorbance')
grid on
```

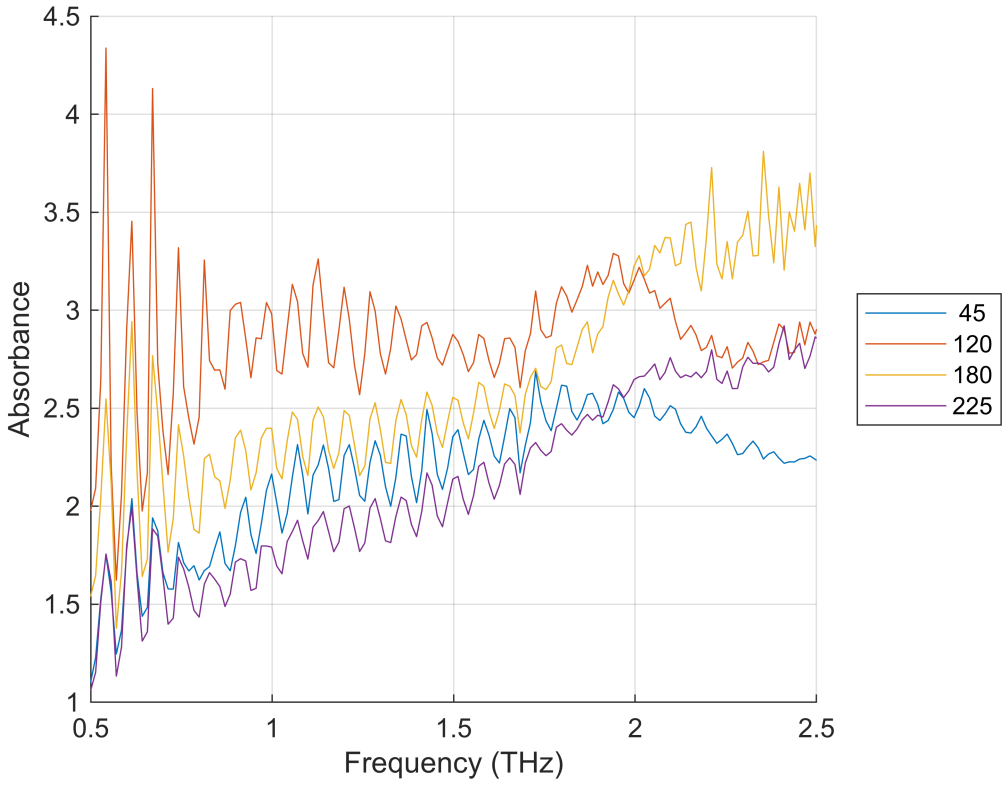

Sine Fit Function:

```
function [fit,amplitude, phase, offset,error] = fitsine(signal, angle)
%Function assumes that the data collected has zero degrees for the first
%sample and 360 for the last.  The sample at 360 is dropped as the optimum
%fit assumes a single cycle.
a=2*mean(signal(1:end-1).*sin(4*pi*angle(1:end-1)/360));
b=2*mean(signal(1:end-1).*cos(4*pi*angle(1:end-1)/360));
amplitude=sqrt(a^2+b^2);
phase=atan2(b,a);
offset=mean(signal);
fit.angle=linspace(0,360,1000);
fit.data=amplitude*sin(4*pi*fit.angle/360+phase)+offset;
temp=amplitude*sin(4*pi*angle/360+phase)+offset;
```

```
error=signal-temp;


end
```

References

[1] Erik T. Thostenson, Zhifeng Ren, and Tsu-Wei Chou. Advances in the science and technology of carbon nanotubes and their composites: a review. *Composites Science and Technology*, 61(13):1899–1912, 2001.

[2] Robert C. Haddon. Carbon Nanotubes. *Accounts of Chemical Research*, 35(12):997–997, December 2002. Publisher: American Chemical Society.

[3] Prabira Sethy, Sethy Pratyush, Ranjan Mishra, and Santi Behera. An Introduction to Terahertz Technology, Its History, Properties and Application. February 2015.

[4] Ashok K. Singh. Chapter 2 - Structure, Synthesis, and Application of Nanoparticles. In Ashok K. Singh, editor, *Engineered Nanoparticles*, pages 19–76. Academic Press, Boston, 2016.

[5] Liu Wei, Liu Yu, Huang Jiaoqi, Huang Guorong, Zhang Yang, and Fu Weiling. Application of terahertz spectroscopy in biomolecule detection. *Frontiers in Laboratory Medicine*, 2(4):127–133, 2018.

[6] Sumio Iijima. Helical microtubules of graphitic carbon. *Nature*, 354(6348):56–58, November 1991.

[7] Abd El-Moez A. Mohamed and Mohamed A. Mohamed. 2 - Carbon nanotubes: Synthesis, characterization, and applications. In Kamel A. Abd-Elsalam, editor, *Carbon Nanomaterials for Agri-Food and Environmental Applications*, Micro and Nano Technologies, pages 21–32. Elsevier, 2020.

[8] Min Ouyang, Jin-Lin Huang, and Charles M. Lieber. Fundamental Electronic Properties and Applications of Single-Walled Carbon Nanotubes. *Accounts of Chemical Research*, 35(12):1018–1025, 2002. _eprint: https://doi.org/10.1021/ar0101685.

[9] Hiromu Hamasaki and Kaori Hirahara. The van der Waals cohesive force between two carbon nanotubes. *Applied Physics Express*, 16(3):035002, March 2023. Publisher: IOP Publishing.

[10] V. V. Smirnov and L. I. Manevitch. Carbon Nanotubes in Arrays: Competition of van-der-Waals and Elastic Forces. *Doklady Physics*, 64(5):218–221, May 2019.

[11] Aparna Gangele, Sathish Kumar Garala, and Ashok Kumar Pandey. Influence of van der Waals forces on elastic and buckling characteristics of vertically aligned carbon nanotubes. *International Journal of Mechanical Sciences*, 146-147:191–199, 2018.

[12] Sayan Deb Dutta, Dinesh K. Patel, and Ki-Taek Lim. Chapter 21 - Carbon nanotube-based nanohybrids for agricultural and biological applications. In Kamel A. Abd-Elsalam, editor, *Multifunctional Hybrid Nanomaterials for Sustainable Agri-Food and Ecosystems*, pages 505–535. Elsevier, January 2020.

[13] Khalid Saeed and Ibrahim Khan. Carbon nanotubes-properties and applications: a review. *Carbon letters*, 14, July 2013.

[14] Pavel Nikolaev, Michael J Bronikowski, R.Kelley Bradley, Frank Rohmund, Daniel T Colbert, K.A Smith, and Richard E Smalley. Gas-phase catalytic growth of single-walled carbon nanotubes from carbon monoxide. *Chemical Physics Letters*, 313(1):91–97, November 1999.

[15] Manish Pant, Rahul Singh, Prateek Negi, Kritika Tiwari, and Yashvir Singh. A comprehensive review on carbon nano-tube synthesis using chemical vapor deposition. *International Conference on Technological Advancements in Materials Science and Manufacturing*, 46:11250–11253, January 2021.

[16] Valentin N. Popov. Carbon nanotubes: properties and application. *Materials Science and Engineering: R: Reports*, 43(3):61–102, 2004.

[17] J.-P. Salvetat, J.-M. Bonard, N.H. Thomson, A.J. Kulik, L. Forró, W. Benoit, and L. Zuppiroli. Mechanical properties of carbon nanotubes. *Applied Physics A*, 69(3):255–260, September 1999.

[18] Sayed Abolfazl Mirdehghan. 1 - Fibrous polymeric composites. In Masoud Latifi, editor, *Engineered Polymeric Fibrous Materials*, The Textile Institute Book Series, pages 1–58. Woodhead Publishing, 2021.

[19] John Hone, Marc Llaguno, Norbert Nemes, a t charlie Johnson, J. Fischer, DA Walters, Michael Casavant, J. Schmidt, and R. Smalley. Electrical and Thermal Transport Properties of Magnetically Aligned Single-Wall Carbon Nanotube Films. *Applied Physics Letters*, 77:666–668, July 2000.

[20] Zhidong Han and Alberto Fina. Thermal conductivity of carbon nanotubes and their polymer nanocomposites: A review. *Progress in Polymer Science*, 36(7):914–944, 2011.

[21] Agnieszka Lekawa-Raus, Jeff Patmore, Lukasz Kurzepa, John Bulmer, and Krzysztof Koziol. Electrical Properties of Carbon Nanotube Based Fibers and Their Future Use in Electrical Wiring. *Advanced Functional Materials*, 24(24):3661–3682, June 2014. Publisher: John Wiley & Sons, Ltd.

[22] T. W. Ebbesen, H. J. Lezec, H. Hiura, J. W. Bennett, H. F. Ghaemi, and T. Thio. Electrical conductivity of individual carbon nanotubes. *Nature*, 382(6586):54–56, July 1996.

[23] Sander Tans, Alwin Verschueren, and Cees Dekker. Room-Temperature Transistor Based on a Single Carbon Nanotube. *Nature*, 393:49–52, May 1998.

[24] Mauricio Terrones, Humberto Terrones, M. S. Dresselhaus, G. Dresselhaus, J. C. Charlier, and E. Hernández. Electronic, thermal and mechanical properties of carbon nanotubes. *Philosophical Transactions of the Royal Society of London. Series A: Mathematical, Physical and Engineering Sciences*, 362(1823):2065–2098, 2004. _eprint: https://royalsocietypublishing.org/doi/pdf/10.1098/rsta.2004.1430.

[25] John Robertson. Realistic applications of CNTs. *Materials Today*, 7(10):46–52, October 2004.

[26] S.J. Pennycook. Transmission Electron Microscopy. In Franco Bassani, Gerald L. Liedl, and Peter Wyder, editors, *Encyclopedia of Condensed Matter Physics*, pages 240–247. Elsevier, Oxford, January 2005.

[27] Mohammad Jafari Eskandari, Mohsen Asadi Asadabad, Reza Tafrishi, and Mehdi Emamalizadeh. Transmission electron microscopy characterization of different nanotubes. *Inorganic and Nano-Metal Chemistry*, 47(2):197–201, February 2017. Publisher: Taylor & Francis.

[28] T. Belin and F. Epron. Characterization methods of carbon nanotubes: a review. *Materials Science and Engineering: B*, 119(2):105–118, May 2005.

[29] Vincent Meunier and Philippe Lambin. Scanning tunnelling microscopy of carbon nanotubes. *Philosophical transactions. Series A, Mathematical, physical, and engineering sciences*, 362(1823):2187–2203, October 2004. Place: England.

[30] Firas Habeb Abdulrazzak, Ayad Fadel Alkiam, and Falah Hasan Hussein. Behavior of X-Ray Analysis of Carbon Nanotubes. In Hosam El-Din Saleh and Said Moawad Mohamed El-Sheikh, editors, *Perspective of Carbon Nanotubes*. IntechOpen, Rijeka, 2019. Section: 7.

[31] C. Branca, F. Frusteri, V. Magazù, and A. Mangione. Characterization of Carbon Nanotubes by TEM and Infrared Spectroscopy. *The Journal of Physical Chemistry B*, 108(11):3469–3473, March 2004. Publisher: American Chemical Society.

[32] M.S. Dresselhaus, G. Dresselhaus, R. Saito, and A. Jorio. Raman spectroscopy of carbon nanotubes. *Physics Reports*, 409(2):47–99, March 2005.

[33] Ado Jorio, Marcos Pimenta, Antonio Souza Filho, Riichiro Saito, G Dresselhaus, and M Dresselhaus. Characterizing Carbon Nanotube Samples with Resonance Raman Scattering. *New Journal of Physics*, 5:139, October 2003.

[34] F. Liu, R.M. Wagterveld, B. Gebben, M.J. Otto, P.M. Biesheuvel, and H.V.M. Hamelers. Carbon nanotube yarns as strong flexible conductive capacitive electrodes. *Colloid and Interface Science Communications*, 3:9–12, November 2014.

[35] Md. Milon Hossain, Mostakima M. Lubna, and Philip D. Bradford. Multifunctional and Washable Carbon Nanotube-Wrapped Textile Yarns for Wearable E-Textiles. *ACS Applied Materials & Interfaces*, 15(2):3365–3376, January 2023. Publisher: American Chemical Society.

[36] Alexander E. Bogdanovich and Philip D. Bradford. Carbon nanotube yarn and 3-D braid composites. Part I: Tensile testing and mechanical properties analysis. *Composites Part A: Applied Science and Manufacturing*, 41(2):230–237, February 2010.

[37] Mark J. Schulz, Yi Gang Song, Adam Hehr, and Vesselin N. Shanov. Embedded carbon nanotube thread piezoresistive strain sensor performance. *Sensor Review*, 34:209–219, 2014.

[38] MIRALON®.

[39] SBIR-STTR-Success: Nanocomp Technologies, Inc. | SBIR.gov.

[40] NASA Invites Media to Visit Nanocomp Technologies, Discuss Space Technology Partnership - NASA. Section: NASA Headquarters.

[41] J. K. Chaffee, David S. Lashmore, Diana J. Lewis, Jennifer E. Mann, Mark W. Schauer, and Brian White. Direct Synthesis of CNT Yarns and Sheets. 2008.

[42] Furat Dawood, Martin Anda, and G. M. Shafiullah. Hydrogen production for energy: An overview. *International Journal of Hydrogen Energy*, 45(7):3847–3869, 2020.

[43] The Future of Hydrogen, June 2019.

[44] Rebekah D. Downes, Ayou Hao, Jin Gyu Park, Yi-Feng Su, Richard Liang, Benjamin D. Jensen, Emilie J. Siochi, and Kristopher E. Wise. Geometrically constrained self-assembly and crystal packing of flattened and aligned carbon nanotubes. *Carbon*, 93:953–966, November 2015.

[45] Seiji Kojima. Terahertz Spectroscopy in Advanced Materials Science. In Yahya M. Meziani and Jesús E. Velázquez-Pérez, editors, *Trends in Terahertz Technology*, page Ch. 2. IntechOpen, Rijeka, April 2023.

[46] Peter A. Banks, Elyse M. Kleist, and Michael T. Ruggiero. Investigating the function and design of molecular materials through terahertz vibrational spectroscopy. *Nature Reviews Chemistry*, 7(7):480–495, July 2023.

[47] Katsuhiro Ajito. Terahertz Spectroscopy for Pharmaceutical and Biomedical Applications. *IEEE Transactions on Terahertz Science and Technology*, 5(6):1140–1145, 2015.

[48] Mark H. Bergen, Seth N. Lowry, Michael E. Mitchell, Matthias F. Jenne, Christopher M. Collier, and Jonathan F. Holzman. Terahertz wireless communication systems: challenges and solutions for realizations of effective bidirectional links. *Opt. Continuum*, 2(10):2154–2177, October 2023. Publisher: Optica Publishing Group.

[49] Harry W Baxter, Adam A Worrall, Jie Pang, Riqing Chen, and Bin Yang. Volatile Liquid Detection by Terahertz Technologies. *Frontiers in Physics*, 9, 2021.

[50] F. Ellrich, M. Bauer, N. Schreiner, A. Keil, T. Pfeiffer, J. Klier, S. Weber, J. Jonuscheit, F. Friederich, and D. Molter. Terahertz Quality Inspection for Automotive and Aviation Industries. *Journal of Infrared, Millimeter, and Terahertz Waves*, 41(4):470–489, April 2020.

[51] Mindaugas Karaliūnas, Kinan E. Nasser, Andrzej Urbanowicz, Irmantas Kašalynas, Dalia Bražinskienė, Svajus Asadauskas, and Gintaras Valušis. Non-destructive inspection of food and technical oils by terahertz spectroscopy. *Scientific Reports*, 8(1):18025, December 2018.

[52] Peter Salén, Martina Basini, Stefano Bonetti, János Hebling, Mikhail Krasilnikov, Alexey Y. Nikitin, Georgii Shamuilov, Zoltán Tibai, Vitali Zhaunerchyk, and Vitaliy Goryashko. Matter manipulation with extreme terahertz light: Progress in the enabling THz technology. *Matter manipulation with extreme terahertz light: Progress in the enabling THz technology*, 836-837:1–74, December 2019.

[53] Andreas Wacker, Gerald Bastard, Francesca Carosella, Robson Ferreira, and Emmanuel Dupont. Unraveling of free-carrier absorption for terahertz radiation in heterostructures. *Phys. Rev. B*, 84(20):205319, November 2011. Publisher: American Physical Society.

[54] Matthias M. Wiecha, Rohit Kapoor, and Hartmut G. Roskos. Terahertz scattering-type near-field microscopy quantitatively determines the conductivity and charge carrier density of optically doped and impurity-doped silicon. *APL Photonics*, 6(12):126108, December 2021.

[55] Krzysztof Iwaszczuk, Maksim Zalkovskij, Andrew C. Strikwerda, and Peter U. Jepsen. Nitrogen plasma formation through terahertz-induced ultrafast electron field emission. *Optica*, 2(2):116–123, February 2015. Publisher: Optica Publishing Group.

[56] Ligang Chen, Guanhua Ren, Liyuan Liu, Lu Zhou, Shaoxian Li, Zhongjie Zhu, Jianbing Zhang, Wentao Zhang, Yanfeng Li, Weili Zhang, Hongwei Zhao, and Jiaguang Han. Probing lattice vibration of alkali halide crystals by broadband terahertz spectroscopy. *Spectrochimica Acta Part A: Molecular and Biomolecular Spectroscopy*, 254:119671, June 2021.

[57] M. Teich, M. Wagner, D. Stehr, H. Schneider, M. Helm, C. N. Böttge, A. C. Klettke, S. Chatterjee, M. Kira, S. W. Koch, G. Khitrova, and H. M. Gibbs. Systematic investigation of terahertz-induced excitonic Rabi splitting. *Phys. Rev. B*, 89(11):115311, March 2014. Publisher: American Physical Society.

[58] Shinichi Watanabe, Nobutsugu Minami, and Ryo Shimano. Intense terahertz pulse induced exciton generation in carbon nanotubes. *Optics Express*, 19(2):1528–1538, January 2011. Publisher: Optica Publishing Group.

[59] Matthew C. Beard, Gordon M. Turner, and Charles A. Schmuttenmaer. Terahertz Spectroscopy. *The Journal of Physical Chemistry B*, 106(29):7146–7159, July 2002. Publisher: American Chemical Society.

[60] Jason B. Baxter and Glenn W. Guglietta. Terahertz Spectroscopy. *Analytical Chemistry*, 83(12):4342–4368, June 2011. Publisher: American Chemical Society.

[61] Jens Neu and Charles A. Schmuttenmaer. Tutorial: An introduction to terahertz time domain spectroscopy (THz-TDS). *Journal of Applied Physics*, 124(23):231101, December 2018.

[62] Withawat Withayachumnankul and Mira Naftaly. Fundamentals of Measurement in Terahertz Time-Domain Spectroscopy. *Journal of Infrared, Millimeter, and Terahertz Waves*, 35(8):610–637, August 2014.

[63] Mira Naftaly, Nico Vieweg, and Anselm Deninger. Industrial Applications of Terahertz Sensing: State of Play. *Sensors*, 19(19), 2019.

[64] Ping Ye, Qinghao Meng, Guoyang Wang, Haiyun Huang, Yizhou Yang, Bo Su, and Cunlin Zhang. Terahertz spectroscopic detection of amino acid molecules under magnetic field. *Heliyon*, 8(11):e11414, November 2022. Place: England.

[65] Ashish Y. Pawar, Deepak D. Sonawane, Kiran B. Erande, and Deelip V. Derle. Terahertz technology and its applications. *Drug Invention Today*, 5(2):157–163, 2013.

[66] Kiarash Ahi, Sina Shahbazmohamadi, and Navid Asadizanjani. Quality control and authentication of packaged integrated circuits using enhanced-spatial-resolution terahertz time-domain spectroscopy and imaging. *Optical Tools for Metrology, Imaging and Diagnostics*, 104:274–284, May 2018.

[67] Christopher D. Stoik, Matthew J. Bohn, and James L. Blackshire. Nondestructive evaluation of aircraft composites using transmissive terahertz time domain spectroscopy. *Opt. Express*, 16(21):17039–17051, October 2008. Publisher: Optica Publishing Group.

[68] Martin Koch, Daniel M. Mittleman, Jan Ornik, and Enrique Castro-Camus. Terahertz time-domain spectroscopy. *Nature Reviews Methods Primers*, 3(1):48, June 2023.

[69] Mathias Hedegaard Kristensen, Emilie Herault, Dongwei Zhai, Esben Skovsen, and Jean-Louis Coutaz. Terahertz generation through optical rectification in reflection. *Journal of Applied Physics*, 133(17):173103, May 2023.

[70] H. Hamster, A. Sullivan, S. Gordon, W. White, and R. W. Falcone. Subpicosecond, electromagnetic pulses from intense laser-plasma interaction. *Phys. Rev. Lett.*, 71(17):2725–2728, October 1993. Publisher: American Physical Society.

[71] Wenfeng Sun, Xinke Wang, and Yan Zhang. Terahertz generation from laser-induced plasma. *Opto-Electronic Science*, 1(8):220003–1, 2022. Num Pages: 220003-27.

[72] David G. Cooke. Terahertz Photoconductivity. In *Photoconductivity and Photoconductive Materials*, pages 369–398. John Wiley & Sons, Ltd, 2022. Section: 9 _eprint: https://onlinelibrary.wiley.com/doi/pdf/10.1002/9781119579182.ch9.

[73] Evangelos Th Papaioannou and René Beigang. THz spintronic emitters: a review on achievements and future challenges. *Nanophotonics*, 10(4):1243–1257, 2021.

[74] T. Seifert, S. Jaiswal, U. Martens, J. Hannegan, L. Braun, P. Maldonado, F. Freimuth, A. Kronenberg, J. Henrizi, I. Radu, E. Beaurepaire, Y. Mokrousov, P. M. Oppeneer, M. Jourdan, G. Jakob, D. Turchinovich, L. M. Hayden, M. Wolf, M. Münzenberg, M. Kläui, and T. Kampfrath. Efficient metallic spintronic emitters of ultrabroadband terahertz radiation. *Nature Photonics*, 10(7):483–488, July 2016.

[75] D. H. Auston, K. P. Cheung, and P. R. Smith. Picosecond photoconducting Hertzian dipoles. *Applied Physics Letters*, 45(3):284–286, August 1984.

[76] Jean-Louis Coutaz, Frederic Garet, and Vincent P. Wallace. *Principles of Terahertz Time-Domain Spectroscopy*. Pan Stanford Publishing, an imprint of Pan Stanford, Singapore, first edition. edition, 2018. Publication Title: Principles of Terahertz Time-Domain Spectroscopy.

[77] Kai-Erik. Peiponen, Axel. Zeitler, and Makoto. Kuwata-Gonokami. *Terahertz Spectroscopy and Imaging*. Springer Series in Optical Sciences, 171. Springer Berlin Heidelberg, Berlin, Heidelberg, 1st ed. 2013. edition, 2013.

[78] Nathan M. Burford and Magda O. El-Shenawee. Review of terahertz photoconductive antenna technology. *Optical Engineering*, 56(1):010901, 2017. Publisher: SPIE.

[79] David R. Bacon, Julien Madéo, and Keshav M. Dani. Photoconductive emitters for pulsed terahertz generation. *Journal of Optics*, 23(6):064001, April 2021. Publisher: IOP Publishing.

[80] Jitao Zhang, Mingguang Tuo, Min Liang, Xiong Wang, and Hao Xin. Contribution assessment of antenna structure and in-gap photocurrent in terahertz radiation of photoconductive antenna. *Journal of Applied Physics*, 124(5):053107, August 2018.

[81] F. Sizov and A. Rogalski. THz detectors. *Progress in Quantum Electronics*, 34(5):278–347, September 2010.

[82] Xi-Cheng. Zhang and Jingzhou. Xu. *Introduction to THz Wave Photonics*. Springer US, New York, NY, 2010. Publication Title: Introduction to THz Wave Photonics.

[83] Peter Uhd Jepsen. Phase Retrieval in Terahertz Time-Domain Measurements: a "how to" Tutorial. *Journal of Infrared, Millimeter, and Terahertz Waves*, 40(4):395–411, April 2019.

[84] Kateryna Kushnir. *Microscopic conductivity and ultrafast photocurrents in chalcogenides from 2D to 3D and beyond*. PhD thesis, Worcester Polytechnic Institute, August 2021.

[85] Ziran Wu, Lu Wang, Yitian Peng, Abram Young, Supapan Seraphin, and Hao Xin. Terahertz characterization of multi-walled carbon nanotube films. *Journal of Applied Physics*, 103(9):094324, May 2008.

[86] Sunil Kumar, Natrajan Kamaraju, Alexander Moravsky, R. O. Loutfy, Marc Tondusson, Eric Freysz, and Ajay Kumar Sood. Terahertz Time Domain Spectroscopy to Detect Low-Frequency Vibrations of Double-Walled Carbon Nanotubes. *European Journal of Inorganic Chemistry*, 2010(27):4363–4366, September 2010. Publisher: John Wiley & Sons, Ltd.

[87] Alison Rodger. Linear Dichroism. pages 493–523. John Wiley & Sons, Inc, Hoboken, NJ, USA, 2011.

[88] Lei Ren, Cary L. Pint, Layla G. Booshehri, William D. Rice, Xiangfeng Wang, David J. Hilton, Kei Takeya, Iwao Kawayama, Masayoshi Tonouchi, Robert H. Hauge, and Junichiro Kono. Carbon Nanotube Terahertz Polarizer. *Nano Letters*, 9(7):2610–2613, July 2009. Publisher: American Chemical Society.

[89] Lei Ren, Cary L. Pint, Takashi Arikawa, Kei Takeya, Iwao Kawayama, Masayoshi Tonouchi, Robert H. Hauge, and Junichiro Kono. Broadband Terahertz Polarizers with Ideal Performance Based on Aligned Carbon Nanotube Stacks. *Nano Letters*, 12(2):787–790, February 2012. Publisher: American Chemical Society.

[90] Yoshikazu Takeda, Akio Sasaki, Yujiro Imamura, and Toshinori Takagi. Electron mobility and energy gap of In0.53Ga0.47As on InP substrate. *Journal of Applied Physics*, 47(12):5405–5408, December 1976.

[91] N. Vieweg, F. Rettich, A. Deninger, H. Roehle, R. Dietz, T. Göbel, and M. Schell. Terahertz-time domain spectrometer with 90 dB peak dynamic range. *Journal of Infrared, Millimeter, and Terahertz Waves*, 35(10):823–832, October 2014.

[92] *Terahertz Technologies Systems and Accessories*. Toptica Photonics.